












WASP-121 b’s transmission spectrum observed with JWST/NIRSpec G395H reveals thermal dissociation and SiO in the atmosphere

CYRIL GAPP ^a ,^{1,2} THOMAS M. EVANS-SOMA ,^{3,1} JOANNA K. BARSTOW ,⁴ JOSHUA D. LOTHINGER ,^{5,6}
DAVID K. SING ,^{7,8} DJEMMA RUSEVA ,^{1,9} EVA-MARIA AHRER ,¹ JAYESH M. GOYAL ,¹⁰ DUNCAN CHRISTIE ,¹
LAURA KREIDBERG ,¹ AND NATHAN J. MAYNE ¹¹

¹*Max-Planck-Institut für Astronomie, Königstuhl 17, D-69117 Heidelberg, Germany*

²*Department of Physics and Astronomy, Heidelberg University, Im Neuenheimer Feld 226, D-69120 Heidelberg, Germany*

³*School of Information and Physical Sciences, University of Newcastle, Callaghan, NSW, Australia*

⁴*School of Physical Sciences, The Open University, Walton Hall, Milton Keynes, MK7 6AA, UK*

⁵*Space Telescope Science Institute, 3700 San Martin Drive, Baltimore, MD 21218, USA*

⁶*Department of Physics, Utah Valley University, 800 West University Parkway, Orem, UT 84058, USA*

⁷*Department of Earth & Planetary Sciences, Johns Hopkins University, Baltimore, MD, USA*

⁸*Department of Physics & Astronomy, Johns Hopkins University, Baltimore, MD, USA*

⁹*University of St Andrews, North Haugh, St Andrews, KY16 9SS, UK*

¹⁰*School of Earth and Planetary Sciences (SEPS), National Institute of Science Education and Research (NISER), Jatani, India*

¹¹*Department of Physics and Astronomy, Faculty of Environment, Science and Economy, University of Exeter, Exeter EX4 4QL, UK*

ABSTRACT

WASP-121 b has been established as a benchmark ultrahot Jupiter, serving as a laboratory for the atmospheric chemistry and dynamics of strongly irradiated extrasolar gas giants. Here, we present and analyze WASP-121 b’s transmission spectrum observed with NIRSpec G395H on board the James Webb Space Telescope and find evidence for the thermal dissociation of H₂O and H₂ on the planet’s permanent dayside. Additionally, we detect SiO at a statistical significance of 5.2 σ which is compatible with chemical equilibrium in the atmosphere. Constraining the abundance of SiO and abundance ratios between silicon and volatile atoms in WASP-121 b’s atmosphere could help discriminate between possible migration histories of the planet. The three-dimensional nature of thermal dissociation on WASP-121 b’s dayside and of recombination on its nightside, however, poses a challenge to constraining molecular abundances and elemental abundance ratios from the transmission spectrum. To account for this, we implemented an atmospheric model in the NEMESIS framework that splits the planet’s atmosphere into dayside and nightside. A retrieval applying our atmospheric model to WASP-121 b’s transmission spectrum favors a higher H₂O abundance on the nightside than on the dayside, demonstrating the impact of hemispheric heterogeneity when attempting to constrain WASP-121 b’s bulk H₂O inventory.

Keywords: Exoplanet atmospheric composition (2021) — Transmission spectroscopy(2133) — Infrared spectroscopy (2285)

1. INTRODUCTION

WASP-121 b is a gas giant exoplanet with a mass of 1.16 ± 0.07 Jupiter masses and a radius of 1.75 ± 0.04 Jupiter radii that orbits an F-type star with a period of 1.274925 days (Bourrier et al. 2020). At its equilibrium temperature (T_{eq}) of about 2350 K (Delrez et al. 2016), it is classified as an ultrahot Jupiter, because its dayside is hot enough to dissociate most molecules and ionize atoms, fundamentally changing the dynamical and spectroscopic properties of the atmosphere as compared to

planets with $T_{\text{eq}} \lesssim 2000$ K (see, e.g., Bell & Cowan 2018; Parmentier et al. 2018; Lothringer et al. 2020; Beltz et al. 2021). Since most chemical elements are expected to be vaporized in the extreme temperatures of ultrahot Jupiters (see, e.g., Kitzmann et al. 2018; Lothringer et al. 2018), WASP-121 b offers the opportunity to constrain the abundances of its constituent species using atmospheric observations. This opens up a promising path to infer its formation history, because the amount of rocky material accreted during the planet’s forma-

tion and eventual migration can be inferred from its refractory-to-volatile elemental abundance ratios (see, e.g., [Lothringer et al. 2021](#)). Measuring these ratios simultaneously with other elemental abundance ratios, such as the carbon-to-oxygen ratio (C/O), delivers leverage into constraining the planet’s formation location in the protoplanetary disk.

As an exoplanet outstandingly suitable for atmospheric characterization, WASP-121 b has been regularly observed using both ground-based and space-based observatories. Eclipse observations with the Hubble Space Telescope (HST) have revealed a thermal inversion on its permanent dayside ([Evans et al. 2017](#); [Mikal-Evans et al. 2019](#); [Mikal-Evans et al. 2020](#)), implying the existence of short-wavelength absorbers in the atmosphere (see, e.g., [Burrows et al. 2008](#); [Fortney et al. 2008](#)). This has been confirmed by WASP-121 b’s transmission spectrum from the near-ultraviolet (NUV) to the optical observed with HST which revealed a rise in transit depth toward shorter wavelengths in the NUV ([Evans et al. 2018](#)). [Evans et al. \(2018\)](#) were not able to identify any individual short-wavelength absorber conclusively using these observations; however, they suggested VO as a possible optical absorber, did not find evidence for TiO and noted that SH might have caused the observed NUV rise. Ground-based observations of WASP-121 b obtained using HARPS have suggested the presence of neutral vanadium that could give rise to VO ([Hoeijmakers et al. 2020](#)), while atomic titanium and TiO have been ruled out using high-resolution ESPRESSO spectra ([Hoeijmakers et al. 2024](#)), lending plausibility to the suggestion of [Evans et al. \(2018\)](#). [Lothringer et al. \(2022\)](#) argued that the observed NUV rises in WASP-121 b ($T_{\text{eq}} \sim 2350$ K) and WASP-178 b ($T_{\text{eq}} \sim 2450$ K) might be related to the absence of such a rise in HAT-P-41 b ($T_{\text{eq}} \sim 1950$ K) via the condensation of silicate clouds in gas giants with equilibrium temperatures below ~ 2100 K. In that picture, the NUV rises in WASP-121 b and WASP-178 b would not be created by SH, but instead by either SiO or Mg I and Fe II in tandem, while any silicon and magnesium in HAT-P-41 b would be condensed into silicate clouds. Neither Mg I, Fe II or SiO could be identified unambiguously in either WASP-121 b or WASP-178 b, though, due to their overlapping opacities in the NUV. The definite identification of the absorber creating the NUV rise in WASP-121 b has since been pending.

Since WASP-121 b is a highly irradiated, tidally-locked planet, the atmospheric temperatures are dramatically higher on its dayside than on its nightside ([Mikal-Evans et al. 2022, 2023](#)). This difference in temperatures probably drives chemical differences between

the two hemispheres, because the dayside is hot enough to dissociate most molecules, including H_2 , while the temperatures on the nightside are low enough for dissociated species to recombine. Indeed, phase-curve observations of WASP-121 b obtained with HST have revealed stratospheric dayside temperatures high enough to dissociate H_2O , while the nightside temperatures are too low for the thermal dissociation of H_2O ([Mikal-Evans et al. 2022](#)). In line with these phase-curve observations, high-resolution transit observations of WASP-121 b using Gemini-S/IGRINS revealed that the observed H_2O absorption lines moved toward longer wavelengths with time ([Wardenier et al. 2024](#)) which suggests a higher H_2O abundance on the nightside than on the dayside ([Wardenier et al. 2023](#)). In contrast, the observed CO absorption lines became increasingly blueshifted during the observed transits, indicating that CO, unlike H_2O , is abundant on the dayside. These findings are in agreement with predictions from general circulation models (GCMs) of a depletion of H_2O on WASP-121 b’s dayside due to thermal dissociation and a nearly globally uniform distribution of CO which is expected to be stable enough to avoid dissociation ([Parmentier et al. 2018](#)).

This dichotomy between the global distributions of H_2O and CO abundances probably does not only impact phase-curve and high-resolution observations of WASP-121 b, but also low-resolution transmission spectra as the stellar light that filters through the planet’s extended atmosphere during transits probes parts of both the dayside and the nightside (see, e.g., [Caldas et al. 2019](#)). WASP-121 b’s dayside is substantially inflated over the nightside due to its much higher temperatures and lower mean molecular weight caused by the thermal dissociation of H_2 into atomic hydrogen. Thus, the amplitude of absorption bands of any molecule that is abundant on the dayside, such as CO, will be increased, while the absorption amplitudes of molecules that are more abundant on the nightside, such as H_2O , will be decreased. Neglecting these hemispheric differences in a one-dimensional model that prescribes spherical symmetry can thus lead to an overestimation of the planet’s CO abundance and an underestimation of the H_2O abundance, leading to a C/O that is biased to higher values ([Pluriel et al. 2020](#)).

2. OBSERVATION AND DATA REDUCTION

In this work, we analyze a transit of WASP-121 b observed as part of the phase-curve observations of James Webb Space Telescope (JWST) program GO-1729 (PI: Evans-Soma, co-PI: Kataria). The observation was carried out with the NIRSpec instrument employing G395H to obtain spectra between 2.54 and 5.15 μm with a wave-

length gap ranging from 3.72 to 3.82 μm caused by the offset between NIRSpec’s NRS1 and NRS2 detectors. As reported in Mikal-Evans et al. (2023), the telescope pointing and performance throughout the 37.8 hr long phase-curve observation were very stable. A data reduction of the full phase-curve observation including the transit is presented by Evans-Soma et al. (2025) and here, we analyze the transit separately.

2.1. Transit-only analysis

We extracted the target spectrum for each integration of the observation from the respective images using the FIREFLY code (Rustamkulov et al. 2022, 2023) as previously outlined in Mikal-Evans et al. (2023). To obtain WASP-121 b’s transmission spectrum, we analyzed the data from 3.5 hr before to 3.5 hr after the transit midtime, leaving about 2.05 hr of both pre- and post-transit baseline for calibrating stellar fluxes and instrumental systematics in addition to the transit with a duration of about 2.9 hr itself. Compared to a pure transit observation, our transit-only analysis of the phase-curve data has the advantage of the exposure beginning many hours prior to the transit, allowing plenty of time for preliminary settling systematics to subside.

For the analysis of the transit light curves we fit a model of the form

$$M(c_0, c_1, c_2, \theta, t) = B(c_0, c_1, c_2, t)T(\theta, t), \quad (1)$$

to the data in each wavelength bin. Here,

$$B(c_0, c_1, c_2, t) = c_0 + c_1 t + c_2 t^2 \quad (2)$$

is a quadratic baseline incorporating both stellar and planetary fluxes as well as instrumental systematics and $T(\theta, t)$ is a transit model calculated using the `batman` package (Kreidberg 2015). The parameters θ of the transit model we chose are two stellar limb darkening coefficients (u_1 and u_2), the planet’s orbital period (P), eccentricity (ϵ), inclination (i), semi-major axis relative to the star’s radius (a/R_*), and radius relative to the star’s radius (R_p/R_*); and the midtime of the transit (T_{mid}). For all models, we fixed WASP-121 b’s argument of periapsis to 90° , its orbital eccentricity to 0, and its orbital period to 1.27492504 days, as was reported by Bourrier et al. (2020).

To refine orbital parameters that are independent of the observed wavelengths but important for transit observations, we wavelength-integrated the light curves over the NRS1 and NRS2 detectors separately to create two white light curves we then analyzed jointly. We fit the two white light curves simultaneously using the transit model (Equation 1), employing the same orbital

inclination and semi-major axis for both light curves and varying all other transit model and baseline parameters between the two light curves. We first conducted a preliminary least-squares fit and then performed sigma clipping, removing all data points that deviated from the preliminary model by more than 5σ . This sigma clipping only resulted in the removal of one out of 650 data points of the NRS1 light curve and no removed data point of the NRS2 light curve. Then, we ran another least-squares fit and used the Markov-chain Monte Carlo (MCMC) package `emcee` (Foreman-Mackey et al. 2013) to sample the parameters’ posterior distributions, including a systematic white noise term (σ_{sys}), which was added to the Poisson data uncertainties derived from the reduction pipeline in quadrature. For the MCMC, we set wide uniform priors on all model parameters except for the quadratic limb darkening coefficients, for which we adopted normal priors from the `ExoTIC-LD` package (Grant & Wakeford 2022) using the three-dimensional Stagger stellar grid (Magic et al. 2015). The resulting white light curve data and maximum likelihood (ML) models are shown in Figure 1, the parameters’ posteriors are shown in Figure 12 and the parameters’ priors and posterior distributions are summarized in Table 1.

After modeling the white light curves, we divided the time series of the one-dimensional spectra into finer wavelength bins to generate spectrophotometric light curves. We generated these light curves at two different wavelength binning levels: first, binning over 10 detector pixel columns per spectroscopic channel, leading to a spectral resolution of $R \sim 600$ and second, binning over two detector pixel columns, which results in a spectral resolution of $R \sim 3000$, both resolutions varying with wavelength. Finally, we fit the transit model (Equation 1) to each light curve individually, fixing the semi-major axis and orbital inclination to their ML values from the white light curve fit. Thus, the fit parameters for the spectrophotometric light curves were the baseline parameters (c_0 , c_1 and c_2) as well as the planetary radius relative to the stellar radius (R_p/R_*), the transit midtime (T_{mid}) and the two limb darkening coefficients (u_1 and u_2). As in the white light curves’ fit, we first fit the light curves using a least-squares approach, performed sigma clipping with a five sigma threshold and conducted another least-squares fit. The number of sigma-clipped data points for each spectrophotometric light curve is shown in Figure 13. Then, we explored the parameter posteriors using MCMC for which we adopted normal priors calculated using the `ExoTIC-LD` package for the limb darkening coefficients and set wide uniform priors on all other parameters (as in the white

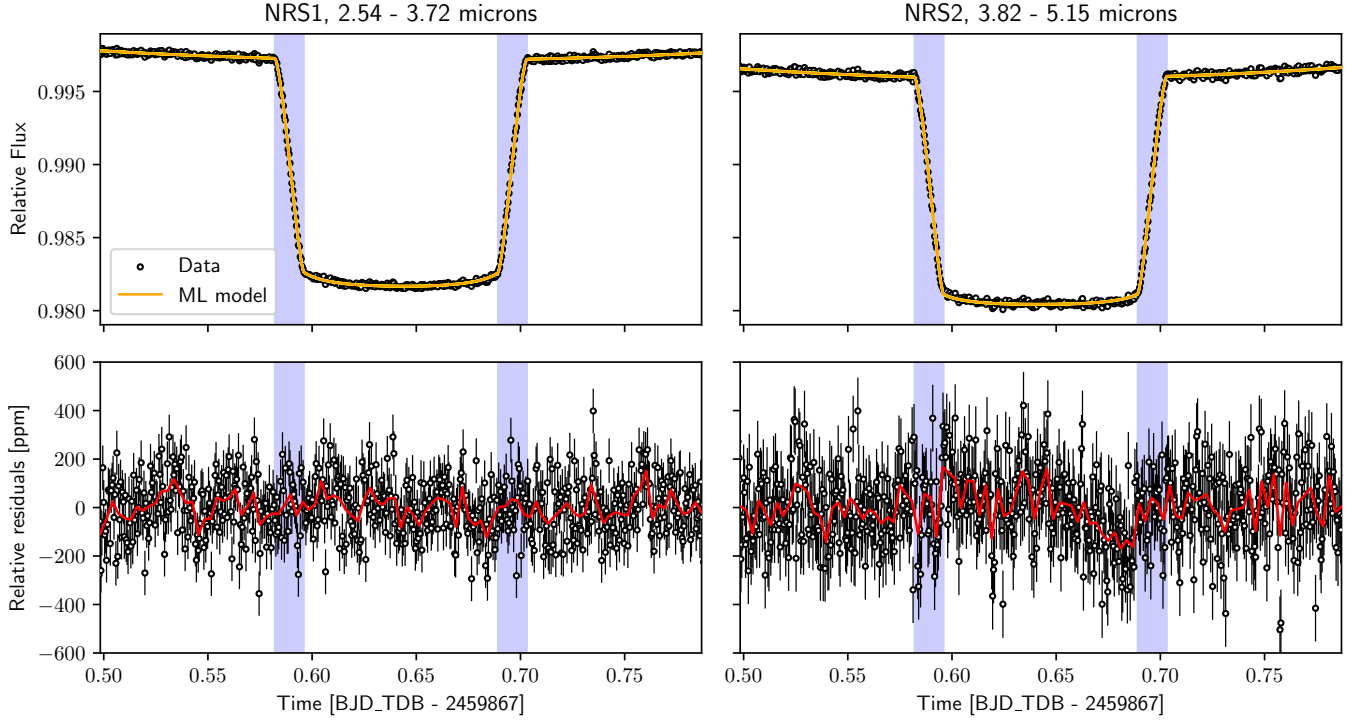


Figure 1. Results of the simultaneous MCMC on the white transit-only light curves of the NRS1 (*left panels*) and NRS2 (*right panels*) detectors. The shaded blue regions indicate the times of ingress and egress calculated according to Winn (2010). *Top panels:* the black circles show the data and the orange lines show the model light curves applying the ML set of parameters. The faint yellow lines show models calculated using 100 random draws from the final parameter samples. *Bottom panels:* the relative residuals between the data and the ML model are shown as black circles with the error bars of the data propagated onto the relative residuals. The residuals binned to a lower resolution in time are plotted using red solid lines.

Table 1. Inputs and results for the light-curve model parameters for fitting the white light curves using MCMC.

Parameter	Description	Detector	Prior	Posterior
a/R_*	Ratio of the semi-major axis to the star's radius	Joint	$\mathcal{U}(0, \infty)$	$3.7844^{+0.0068}_{-0.0068}$
i	Orbital inclination	Joint	$\mathcal{U}(0^\circ, 90^\circ)$	$(87.45^{+0.19}_{-0.18})^\circ$
T_{mid}	Transit midtime [BJD_TDB-2459867]	NRS1	$\mathcal{U}(-\infty, \infty)$	$0.642602^{+0.000014}_{-0.000014}$
T_{mid}	Transit midtime [BJD_TDB-2459867]	NRS2	$\mathcal{U}(-\infty, \infty)$	$0.642552^{+0.000018}_{-0.000018}$
R_p/R_*	Ratio of the planet's to the star's radius	NRS1	$\mathcal{U}(-\infty, \infty)$	$0.122542^{+0.000077}_{-0.000077}$
R_p/R_*	Ratio of the planet's to the star's radius	NRS2	$\mathcal{U}(-\infty, \infty)$	$0.123180^{+0.000093}_{-0.000093}$
u_1	Linear limb darkening coefficient	NRS1	$\mathcal{N}(0.066, 0.012)$	$0.0479^{+0.0059}_{-0.0060}$
u_1	Linear limb darkening coefficient	NRS2	$\mathcal{N}(0.056, 0.009)$	$0.0286^{+0.0058}_{-0.0057}$
u_2	Quadratic limb darkening coefficient	NRS1	$\mathcal{N}(0.11, 0.02)$	$0.102^{+0.010}_{-0.010}$
u_2	Quadratic limb darkening coefficient	NRS2	$\mathcal{N}(0.092, 0.012)$	$0.0819^{+0.0094}_{-0.0095}$
c_0	Constant baseline coefficient (see Equation 1)	NRS1	$\mathcal{U}(-\infty, \infty)$	$1.00881^{+0.00046}_{-0.00045}$
c_0	Constant baseline coefficient (see Equation 1)	NRS2	$\mathcal{U}(-\infty, \infty)$	$1.00977^{+0.00059}_{-0.00059}$
c_1	Linear baseline coefficient (see Equation 1)	NRS1	$\mathcal{U}(-\infty, \infty)$	$-0.0358^{+0.0014}_{-0.0015}$
c_1	Linear baseline coefficient (see Equation 1)	NRS2	$\mathcal{U}(-\infty, \infty)$	$-0.0435^{+0.0019}_{-0.0019}$
c_2	Quadratic baseline coefficient (see Equation 1)	NRS1	$\mathcal{U}(-\infty, \infty)$	$0.0274^{+0.0011}_{-0.0011}$
c_2	Quadratic baseline coefficient (see Equation 1)	NRS2	$\mathcal{U}(-\infty, \infty)$	$0.0341^{+0.0015}_{-0.0015}$
σ_{sys}	Systematic noise term	NRS1	$\mathcal{U}(0, \infty)$	$(70.3^{+5.3}_{-5.3})$ ppm
σ_{sys}	Systematic noise term	NRS2	$\mathcal{U}(0, \infty)$	$(65.9^{+9.7}_{-10.4})$ ppm

NOTE—Uncertainties reported here are 1σ . In the prior column, \mathcal{N} stands for a Gaussian with μ and σ given in parentheses and \mathcal{U} is a uniform prior with the lower and upper edges given in parentheses.

light curves' fit; see Table 1). A selection of the spectrophotometric light curves at $R \sim 600$ and the respec-

tive light-curve models adopting the median values of all parameters are plotted in Figure 2. The Allan deviation plots for both the $R \sim 600$ and $R \sim 3000$ transit light curves are shown in Figure 3 and the posteriors for all fit parameters of all light curves are plotted in Figure 13.

To examine the impact of fitting for the transit midtime in the spectrophotometric light curves, we also ran a separate fit of both the white and spectrophotometric light curves with a joint transit midtime in the white light curves’ fit and fixed the transit midtimes of the spectrophotometric light curves to the white light curve fit’s ML value. This only changed the medians of the transit depths by $< 0.5\sigma$ and the size of the error bars by ~ 0.1 ppm and thus, we analyze the transmission spectrum with free transit midtimes here.

2.2. Comparison between transit-only and phase-curve analysis

WASP-121 b’s transmission spectra derived from our transit-only analysis and presented as part of the phase-curve analysis (Evans-Soma et al. 2025) are depicted in Figure 4 along with the residuals between them. The overall shape of both spectra is very similar; however, there are two notable differences between them: First, the transit-only analysis generally returns smaller transit depths and this offset increases with wavelength (see Figure 4, lowest panels). And second, the uncertainties of the transit-only transmission spectrum are about 70% larger than the ones of the phase-curve transmission spectrum (see Figure 4, middle panels).

In the transit-only analysis, the increasing underestimation of the transit depth with wavelength as compared to the phase-curve analysis (see Figure 4, lower panels) most likely originates in the contamination of the transit light curves with the planet’s nightside emission. In the phase-curve analysis, the planet’s emission as a function of phase is accounted for while the transit-only analysis has no leverage into separating stellar and planetary fluxes, leading to a bias toward lower transit depths that gets stronger with an increasing planetary-to-stellar flux ratio (see, e.g., Kipping & Tinetti 2010). As the planetary-to-stellar flux ratio generally increases with wavelength, this effect leads to greater underestimation of the transit depth with wavelength. To estimate the amplitude of the transit depth underestimation of our transit-only analysis, we fit first-order polynomials to the residuals between both reduction pipelines’ transmission spectra. For $R \sim 600$ ($R \sim 3000$), the fit line goes from about -35 ppm (-47 ppm) at $\lambda = 2.73 \mu\text{m}$ to ≈ -193 ppm (-174 ppm) at $\lambda = 5.17 \mu\text{m}$. For WASP-121 b’s transmission spec-

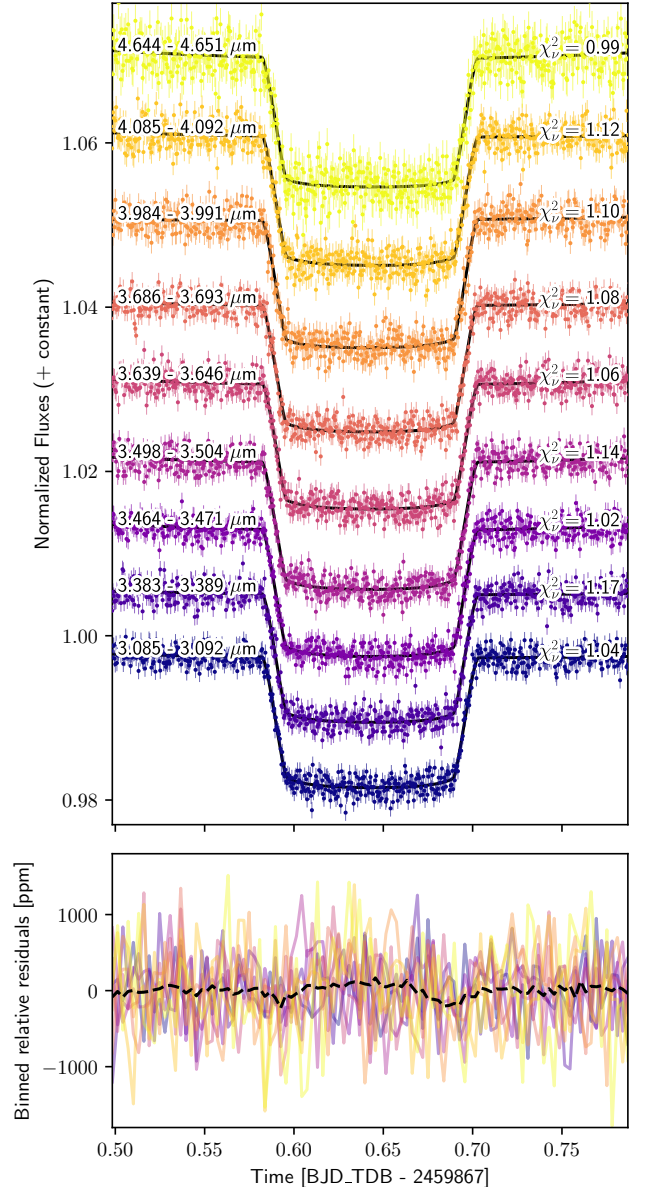


Figure 2. Selection of the spectrophotometric transit-only light curves at a spectral resolution of $R \sim 600$ and respective models. The selected spectrophotometric light curves are the 10th, 20th, 30th, 40th, 50th, 60th, 70th, 80th, and 90th percentile light curves in χ^2_{ν} . *Upper panel:* colored dots with error bars show the data and solid black lines depict the model light curves generated employing the median values of the parameters’ samples explored using MCMC. The wavelength ranges over which the light curves were integrated are given on the left and the χ^2_{ν} of each model fit is given on the right. *Lower panel:* the relative residuals between the selected data and the models binned to a lower resolution in time are shown using solid lines in the color that corresponds to the light curve in the upper panel they belong to. The dashed black line shows the median of the binned residuals of all spectrophotometric light curves (not just the ones plotted in the upper panel).

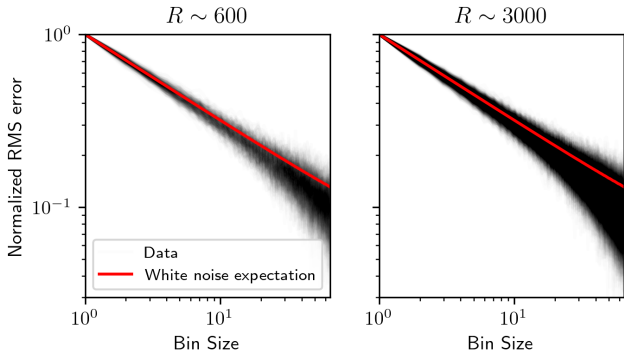


Figure 3. Allan deviation plots for the spectrophotometric transit-only light curves at both spectral resolutions. The transparent black lines show the root mean square (rms) residuals between the data and the models as a function of the number of bins and the red lines show the rms that would be expected if there were only white noise in the data.

trum observed with JWST/NIRSpec, [Morello et al. \(2021\)](#) estimated the bias introduced by nightside emission to be about (266 ± 127) ppm, which depends on the adopted model parameters such as the planet’s nightside temperature. As the difference in transit depths between our two data reductions increases with wavelength and comes out at a similar magnitude as estimated by [Morello et al. \(2021\)](#), the bias introduced by the planet’s nightside emission is likely the dominant source of the observed wavelength-dependent offset.

For both resolutions $R \sim 600$ and $R \sim 3000$, the uncertainties of the transit-only transmission spectrum are $\sim 70\%$ larger than the phase-curve transmission spectrum’s uncertainties (see Figure 4, middle panels). To examine the origin of the size of the error bars, we ran the transit-only analysis with one fitting parameter (either T_{mid} , u_1 , u_2 , c_2 or σ_{sys} ; see Table 1) fixed at a time and inspected the uncertainties on the transit depth. The only significant decrease of the transit depth uncertainties we observed during that exercise was when c_2 was fixed to zero and thus, when a linear instead of a quadratic baseline was adopted. From this observation, we suspect that the increase of transit depth uncertainties of the transit-only analysis as compared to the phase-curve analysis mainly originates in the correlation between the quadratic baseline and the transit depth. In the posteriors of the white light curve fit (Figure 12), there is a clear negative correlation between c_2 and R_p/R_* , meaning that a curvier baseline leads to a smaller planetary radius as a curvier baseline reaches lower fluxes during the transit. This correlation appears to be strong enough to overwhelm the correlation between c_0 and R_p/R_* , which is negative in our posteriors (see Figure 12), but is positive when a lin-

ear baseline is used. Hence, our hypothesis is that the transit-only analysis with its narrower phase coverage of WASP-121 b’s phase-curve delivers weaker constraints on the phase-curve shape which subsequently propagate onto the transit depth uncertainties via the degeneracy with c_2 . We refrained from neglecting the out-of-transit curvature of the observations by adopting a linear instead of a quadratic baseline into our model (Equation 1), since the light curves cannot be adequately fit with a linear baseline due to the strong curvature (see Figures 1 and 2). In the test run using a linear baseline in the light curve model, we observed a systematic overestimation of the transit depth as compared to the run with a quadratic baseline and an increase of the overestimation with wavelength. This bias is caused by the neglected phase-curve curvature that becomes stronger as the planetary-to-stellar flux ratio increases.

In the following analysis of WASP-121 b’s transmission spectrum, we applied atmospheric retrievals to both the transit-only and the phase-curve transmission spectrum to investigate the impact of the planet nightside emission’s contamination of the light curves and the weaker constraints on the phase-curve in the transit-only analysis. Since the phase-curve analysis, however, uses all taken observations to constrain the planet’s emission as a function of time and the correlated transit depth, we consider that approach preferable and draw conclusions primarily driven by the results of that data reduction.

2.3. Limb asymmetries

When interpreting exoplanet transmission spectra, it has traditionally been assumed that the terminator of the planet is homogeneous. However, with JWST-quality data it may be possible to discern terminator inhomogeneities driven by differences in temperature and chemical composition of the morning and evening terminators of the planets, as recently demonstrated for WASP-39 b ([Espinoza et al. 2024](#)) and WASP-107 b ([Murphy et al. 2024](#)). We wanted to investigate whether a uniform terminator model is a sufficient approach for the atmosphere of WASP-121 b. We explored this by applying an asymmetric model to both the white and the spectroscopic light curves using the package *catwoman* ([Espinoza & Jones 2021](#); [Jones & Espinoza 2022](#)) with the nested sampling algorithm *dynesty* ([Speagle 2020](#)).

The white and spectrophotometric light curves of the transit were extracted from the phase-curve light curves ([Evans-Soma et al. 2025](#)) that were analyzed to correct for planetary emission contamination. The *catwoman* package models the transiting planet as two stacked semicircles with different radii and an angle of rotation between the terminator and the direction of propagation

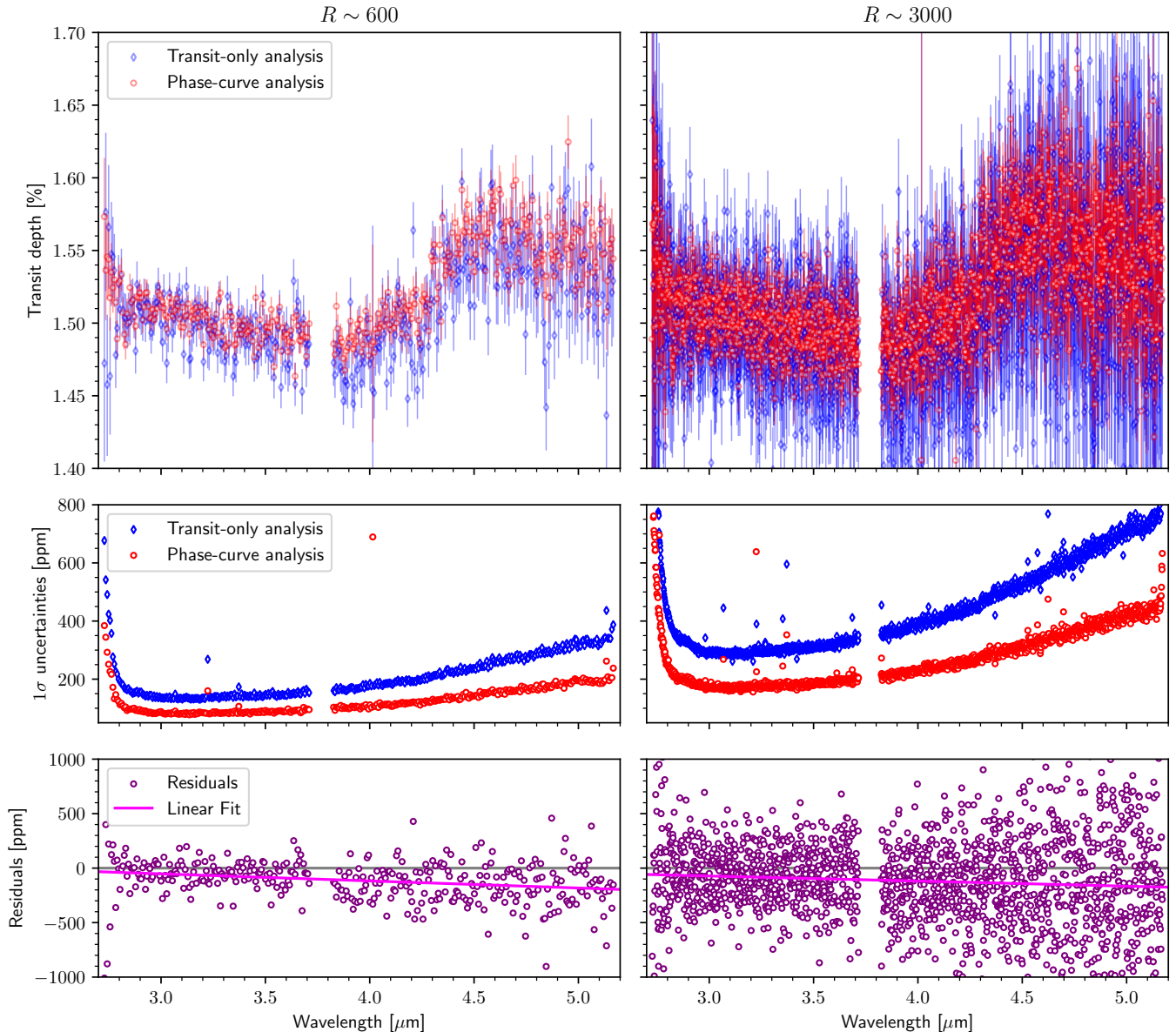


Figure 4. WASP-121 b’s transmission spectra from the transit-only analysis and the phase-curve analysis (Evans-Soma et al. 2025) at two different spectral resolutions. *Upper panels:* the blue diamonds and red circles show the transit-only and phase-curve transmission spectra, respectively. *Middle panels:* the blue diamonds and red circles show the 1σ uncertainties of the transit-only and phase-curve transmission spectra, respectively. *Lower panels:* the purple circles show the transit depths inferred from the transit-only analysis subtracted by the transit depths from the phase-curve analysis. Horizontal gray lines at zero were added to guide the eye. The solid magenta lines present linear fits ($f(\lambda) = c_0 + c_1\lambda$) to the plotted residuals. For $R \sim 600$, $c_0 \approx 142$ ppm and $c_1 \approx -65$ ppm μm^{-1} and for $R \sim 3000$, $c_0 \approx 68$ ppm and $c_1 \approx -47$ ppm μm^{-1} . The spectra displayed in this figure are available for download from the online journal.

of the planet. This angle was set to 90° and a quadratic limb darkening law was assumed. The limb darkening coefficients were obtained from the ExoTIC-LD package (Grant & Wakeford 2022) using the Stagger stellar grid (Magic et al. 2015) and were fixed to those values. We used a semi-major axis of $a/R_* = 3.7844$ and an inclination of 87.45° as reported in Table 1. In the white light curves, we fit the model with a variable transit mid-

time. However, since no significant difference in transit midtime was observed between the `catwoman` and `batman` models, we chose to fix it for the spectroscopic light curves at 2459867.642577 BJD_TDB (see Table 1). We fit a model with two semicircle radii for the morning and evening of the planet, linear and offset terms for the baseline flux, and a systematic noise term. We fixed the integration step scale for the `catwoman` models

to significantly reduce the fitting time. For the default maximum error that is produced by `catwoman` (1 ppm), the optimal integration step scale is `fac = 0.031`. We set it to 0.01 in our fits, which reduces the maximum error in the model by a factor of approximately 10. A smaller integration step scale was explored and it led to a substantial increase in the fitting time, with a negligible decrease in the error bars. We used a total of 1200 live points for each of the model fits.

The Bayesian evidence of the models for the white light curves of the NRS1 and NRS2 detectors (see Figure 14) is shown in Table 2 and demonstrates that the `batman` model is slightly favored in both of the detectors as the Bayes factors are less than one. A comparison between the transmission spectra received from the `batman` and `catwoman` models is presented in Figure 5. Note that the semicircle radii have significantly larger uncertainties due to a strong negative correlation in the posterior (see also, e.g., Espinoza et al. 2024). Additional tests were performed by setting the transit midtime as a free parameter. However, this increased the uncertainties in radius difference even further without any implications on the model comparison. The mean difference between the two radii is 0.006%, showing no evidence of a larger evening atmosphere. Using nested sampling allows us to estimate the Bayesian evidence and compare the two models. For 195 out of 349 spectroscopic light curves, `batman` has higher evidence and for the rest, `catwoman` is preferred, with a maximum logarithmic evidence difference of 2.05, corresponding to a Bayes factor of 7.77, which is not significant enough for us to choose it as the more adequate model. Based on these results, we prefer a symmetric model for the transit-only analysis as there is insufficient evidence for the alternative.

Table 2. Logarithmic Bayesian Evidence for the two models for the light curves from the NRS1 and NRS2 detectors.

	$\ln(Z_1)$	$\ln(Z_2)$	Bayes Factor
NRS1	4106.66	4106.65	0.990
NRS2	3953.19	3952.98	0.811

NOTE— $\ln(Z_1)$ and $\ln(Z_2)$ correspond to the evidence from the `batman` and `catwoman` models, respectively.

3. ATMOSPHERIC MODELS

To identify atmospheric absorbers that contribute to WASP-121 b’s transmission spectrum between 2.7 and 5.2 μm , we analyzed both the phase-curve transmission spectrum and the transit-only transmission spectrum at a spectral resolution of $R \sim 600$ using three different retrieval suites. One of these, the NEMESIS frame-

work, includes an atmospheric model that allows different temperatures and chemistry between the planet’s highly irradiated dayside and the cooler nightside, while the others (`ATMO` and `PETRA`) do not allow differences between hemispheres. Additionally, we compared the phase-curve’s transmission spectrum to model spectra derived from postprocessed output of a GCM presented by Pluriel et al. (2020) to explore the possible impact of WASP-121 b’s three-dimensional nature on the transmission spectrum.

3.1. NEMESIS (Free Chemistry)

NEMESIS is a radiative transfer and retrieval package originally developed for solar system atmospheres, and more recently applied extensively to exoplanets (see, e.g., Lewis et al. 2020; Mikal-Evans et al. 2022). It uses a fast correlated-k framework (Lacis & Oinas 1991) for calculating molecular and atomic opacities, and the nested sampling (Skilling 2004) algorithm PyMultiNest (Feroz et al. 2009; Feroz et al. 2019; Buchner et al. 2014) to sample the parameter space and converge on a solution. For WASP-121 b’s transmission spectrum, we retrieved the abundances of H_2O , CO_2 , CO , SiH , SiO and H^- , for which we adopted the opacity function from Polyansky et al. (2018), Yurchenko et al. (2020), Li et al. (2015), Yurchenko et al. (2018), Barton et al. (2013) and John (1988), respectively. We used $R = 3000$ k tables generated according to Chubb et al. (2021) which were then channel-averaged to the resolution of the data, except for the H^- absorption which is effectively continuum absorption. Additionally, we included collision-induced absorption from H_2 and helium according to Borysow & Frommhold (1989); Borysow & Frommhold (1990), Borysow et al. (1989, 1997, 2001) and Borysow (2002).

To account for the expected thermochemical differences between WASP-121 b’s dayside and nightsides (see Section 1), we implemented an atmospheric model that divides the planet into two hemispheres in the NEMESIS framework (see Figure 6). We allowed the dayside and nightside components in this retrieval setup to have differences in their temperatures as well as their chemistry with the exception of CO , SiO and SiH which we assumed to be constant throughout the planet. For H_2O , H_2 , CO_2 and H^- , we adopted separate dayside and nightside abundances. On the dayside, we additionally allowed H_2 and H_2O to thermally dissociate in the upper atmosphere by parameterizing their abundance profiles using

$$X(P) = \begin{cases} X_{\text{deep}} & \text{if } P \geq P_{\text{knee}} \\ X_{\text{deep}} (P/P_{\text{knee}})^\alpha & \text{else} \end{cases} . \quad (3)$$

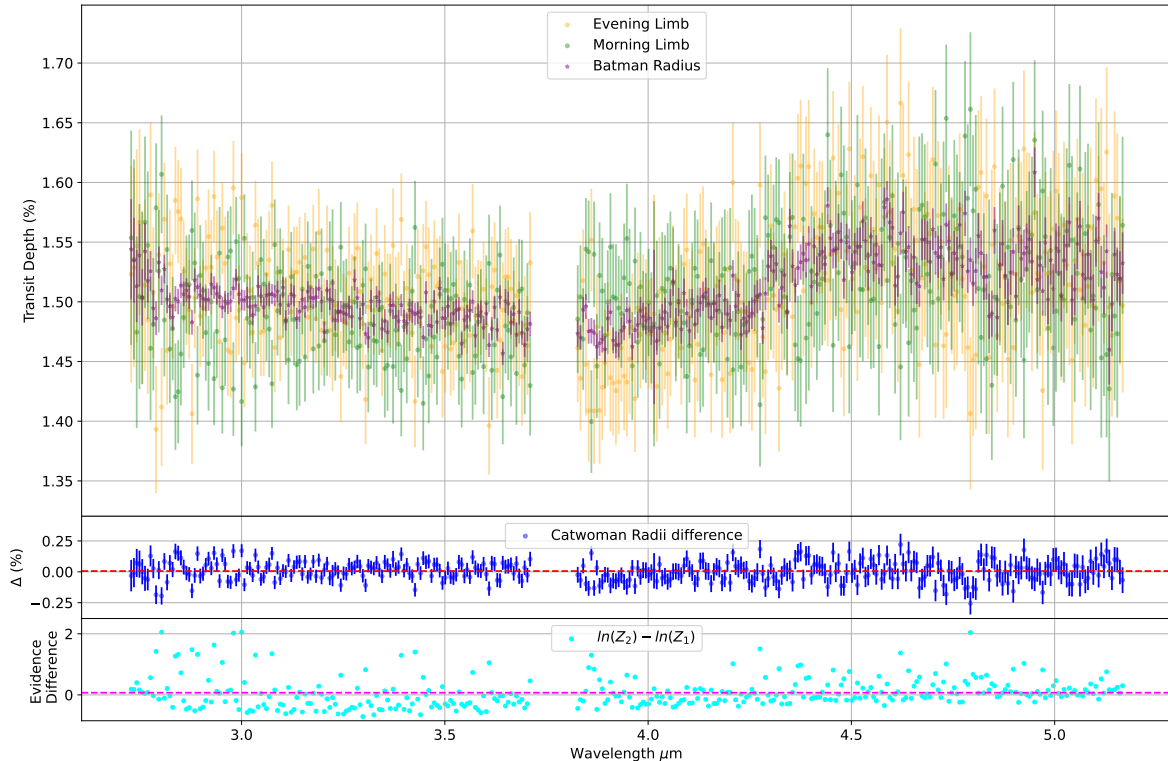


Figure 5. Comparison of the transmission spectra for the *batman* and *catwoman* models. *Top panel:* trailing and leading limb depths compared to the depths found from the *batman* model fitting. *Middle panel:* differences between the trailing and leading limb depths. The red line shows the mean value of 0.006%. *Bottom panel:* difference in logarithmic evidence between the *catwoman* model ($\ln(Z_2)$) and the *batman* model ($\ln(Z_1)$) as estimated from *dynesty*. The pink line shows the mean value of 0.06.

Here, P is pressure, X_{deep} is the molecule’s abundance below the knee pressure level P_{knee} , and α is a power-law index describing the rate at which the abundance decreases with pressure above the knee pressure level. For H_2 , we set $X_{\text{deep}} = 0.8547$, and assumed that all dissociated H_2 is converted to atomic hydrogen, so that the atomic hydrogen abundance increases as H_2 decreases. For H_2O and H_2 on the nightside and for all other molecules, we adopted pressure-independent mole fractions. Finally, we allowed for H^- absorption on the dayside but not on the nightside, and we retrieved the volume mixing ratio of H^- . The free electron volume mixing ratio was fixed to be equal to that of H^- , as was the atomic hydrogen abundance in the deep atmosphere, where it is not augmented by dissociated H_2 .

We modeled the dayside and nightside temperatures using a modified version of the ‘Guillot’ profile (Guillot 2010). The dayside pressure-temperature (P-T) profile was modeled using a reduced three-parameter version of the ‘Guillot’ profile with a single optical stream; retrieved parameters are the infrared opacity ($\kappa_{\text{IR}}^{(\text{day})}$), the ratio of the optical opacity to the infrared opacity ($\gamma^{(\text{day})} = \kappa_{\text{vis}}^{(\text{day})} / \kappa_{\text{IR}}^{(\text{day})}$), and $\beta^{(\text{day})}$ which allows the effective irradiation temperature to be tuned. On the nightside, we made the assumption that $\beta^{(\text{night})}$ must be zero since no irradiation is received from the star; $\gamma^{(\text{night})}$ which governs the optical opacity, is also irrelevant due to the lack of short-wavelength radiation. We

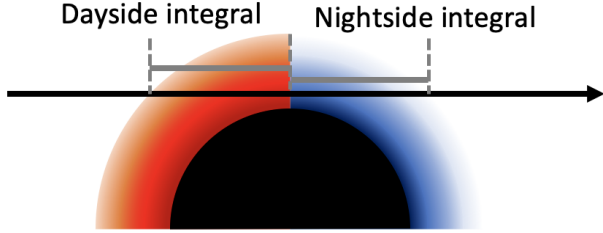


Figure 6. Schematic showing an example path for the NEMESIS dayside-and-nightside radiative transfer calculation. The dayside portion of the atmosphere is represented by shades of red and the nightside by shades of blue. The intensity of the color indicates the atmospheric density, and it can be seen that the density and therefore the pressure on the nightside drop off much more rapidly as a function of altitude. The model altitude coordinate is continuous across the day-night boundary, but the pressure coordinate is not.

therefore described the nightside P-T profile using

$$T(P) = \left(\frac{3}{4} \left(T_{\text{int}} + a^{(1/4)} T_{\text{day}} \right)^4 \left(\frac{2}{3} + \frac{\kappa_{\text{IR}}^{(\text{night})} P}{g} \right) \right)^{(1/4)}, \quad (4)$$

where T_{int} is the internal temperature, set to 500 K, T_{day} is the temperature at the bottom of the model atmosphere on the dayside and the term $a^{(1/4)} T_{\text{day}}$ represents the additional heat advected from the dayside in the deep atmosphere; $\kappa_{\text{IR}}^{(\text{night})}$ is the infrared opacity on the nightside and g is the gravitational acceleration. The two additional free parameters governing the nightside temperature are a , which tunes the amount of extra heat deposited in the deep atmosphere, and $\kappa_{\text{IR}}^{(\text{night})}$. This parameterization does not allow for a thermal inversion on the nightside, however, we consider a noninverted temperature profile on the nightside a reasonable assumption for WASP-121 b, as phase-curve observations using HST have delivered evidence for a decrease of the atmospheric temperature with height on the nightside (Mikal-Evans et al. 2022).

Table 3 lists the priors we chose for all retrieval parameters as well as the posteriors we found in the retrievals on both data reductions’ transmission spectra. For all fit parameters, both retrievals agree remarkably well. The fits to the data are very good for both the retrieval on the phase-curve transmission spectrum (Figure 7) and the retrieval on the transit-only transmission spectrum (Figure 15), with $\chi^2_{\nu} = 1.19$ and $\chi^2_{\nu} = 1.04$, respectively. In both retrievals, we recovered an inverted P-T profile for WASP-121 b’s dayside which increases from $T \sim 2000$ K at $p \sim 100$ mbar to $T \sim 3400$ K at $p \sim 0.1$ mbar (see Figure 8 for the retrieval on the phase-curve transmission spectrum and Figure 16 for the retrieval on the transit-only transmission spectrum). The nightside pro-

file decreases from $T \sim 2000$ K in the deep atmosphere to $T \sim 1350$ K at $p \sim 10$ mbar, and is almost isothermal above this. The retrieved median H_2O abundances are about 6 orders of magnitude lower on the dayside than on the nightside.

To determine which molecules in WASP-121 b’s atmosphere contribute significant opacity to the transmission spectrum, we set the opacity of all molecular absorbers apart from one molecule at a time to zero in the ML model of the retrieval on the phase-curve transmission spectrum and compared the resulting synthetic spectra to the observations (Figure 9). The dominating opacity sources in the NIRSpect G395H bandpass are

1. H_2O , which contributes opacity throughout the entire wavelength range and creates the downward slope of the transmission spectrum between $\lambda \sim 2.7 \mu\text{m}$ and $\lambda \sim 3.7 \mu\text{m}$;
2. SiO which is the strongest opacity source from $\lambda \sim 4.0 \mu\text{m}$ to $\lambda \sim 4.3 \mu\text{m}$; and
3. CO, which dominates the opacities at $\lambda \gtrsim 4.3 \mu\text{m}$ and is responsible for the rise in transit depth at $\lambda \sim 4.6 \mu\text{m}$.

To quantify the statistical significance of SiO in these observations, we performed retrievals in the same setup as before, but without SiO in the atmosphere, and compared the Bayesian evidence of models including and excluding SiO. In the retrieval on the phase-curve transmission spectrum and the retrieval on the transit-only transmission spectrum, respectively, this delivered detection significances of 5.2σ and 2.4σ in favor of the model including SiO.

In addition to our NEMESIS retrieval that splits the planet’s atmosphere along the terminator, we ran a simplified NEMESIS retrieval that does not include heterogeneities between the dayside and nightside of the planet to infer the Bayesian evidence for the new model. For consistency with the approach splitting the atmosphere into dayside and nightside, we kept the power-law profile parameterizations for H_2O and H_2 as well as a constant abundance for H^- and used the three-parameter P-T profile parameterization that was used for the dayside in the more complex model. By comparing the Bayesian evidence between the retrievals on the phase-curve transmission spectrum, we derived a statistical significance of 1.9σ in favor of the atmospheric model that includes dayside and nightside heterogeneities.

3.2. ATMO (Equilibrium Chemistry)

We performed a chemical equilibrium retrieval with ATMO (Amundsen et al. 2014; Tremblin et al. 2015,

Table 3. Inputs and results for the NEMESIS retrieval employing free chemical abundances, split by hemisphere.

Parameter	Hemisphere	Prior	Posteriors	
			PC	TR
WASP-121 b’s radius relative to Jupiter’s radius	Both	$\mathcal{U}(1.2, 2.0)$	$1.69^{+0.01}_{-0.01}$	$1.66^{+0.01}_{-0.01}$
Cloud top pressure in $\log_{10}(\text{bar})$	Both	$\mathcal{U}(-6.0, 1.0)$	$-2.62^{+2.16}_{-2.12}$	$-2.77^{+2.41}_{-1.82}$
Cloud opacity scaling in \log_{10}	Both	$\mathcal{U}(-10.0, 10.0)$	$-4.66^{+3.44}_{-3.22}$	$-4.30^{+2.59}_{-3.02}$
CO mole fraction in \log_{10}	Both	$\mathcal{U}(-12.0, -1.0)$	$-1.08^{+0.05}_{-0.08}$	$-1.27^{+0.11}_{-0.13}$
SiH mole fraction in \log_{10}	Both	$\mathcal{U}(-12.0, -1.0)$	$-8.99^{+1.99}_{-1.82}$	$-8.31^{+1.94}_{-2.35}$
SiO mole fraction in \log_{10}	Both	$\mathcal{U}(-12.0, -1.0)$	$-3.48^{+0.27}_{-0.37}$	$-3.51^{+0.39}_{-0.47}$
a (see Equation 4)	Both	$\mathcal{U}(0.0, 0.15)$	$0.08^{+0.04}_{-0.04}$	$0.09^{+0.04}_{-0.04}$
$\beta^{(\text{day})}$ (see Line et al. 2012, 2013)	Dayside	$\mathcal{U}(0, 2.0)$	$0.85^{+0.19}_{-0.18}$	$0.88^{+0.19}_{-0.17}$
$\gamma^{(\text{day})}$ in \log_{10} (see Guillot 2010; Line et al. 2012, 2013)	Dayside	$\mathcal{U}(-4.0, 3.0)$	$1.18^{+0.60}_{-0.56}$	$1.14^{+0.75}_{-0.65}$
$\kappa_{\text{IR}}^{(\text{day})}$ in \log_{10} (see Guillot 2010; Line et al. 2012, 2013)	Dayside	$\mathcal{U}(-4.0, 3.0)$	$-2.16^{+0.70}_{-0.52}$	$-1.85^{+0.49}_{-0.58}$
Deep atmospheric H_2O mole fraction in \log_{10}	Dayside	$\mathcal{U}(-12.0, -1.0)$	$-8.44^{+2.29}_{-2.21}$	$-7.83^{+2.63}_{-2.49}$
H_2O ’s knee pressure in $\log_{10}(\text{bar})$	Dayside	$\mathcal{U}(-6.0, -1.0)$	$-3.05^{+1.34}_{-1.76}$	$-3.06^{+1.27}_{-1.70}$
H_2O ’s power-law index	Dayside	$\mathcal{U}(0, 3.0)$	$1.45^{+0.91}_{-0.89}$	$1.60^{+0.84}_{-0.93}$
CO_2 ’s mole fraction in \log_{10}	Dayside	$\mathcal{U}(-12.0, -1.0)$	$-8.64^{+1.82}_{-1.99}$	$-8.20^{+2.11}_{-2.35}$
H^- ’s mole fraction in \log_{10}	Dayside	$\mathcal{U}(-13.0, -1.0)$	$-9.09^{+2.38}_{-2.44}$	$-9.01^{+2.11}_{-2.12}$
H_2 ’s knee pressure in $\log_{10}(\text{bar})$	Dayside	$\mathcal{U}(-6.0, -1.0)$	$-3.86^{+1.53}_{-1.26}$	$-4.18^{+1.54}_{-1.10}$
H_2 ’s power-law index	Dayside	$\mathcal{U}(0, 2.0)$	$0.97^{+0.61}_{-0.61}$	$0.92^{+0.58}_{-0.57}$
$\kappa_{\text{IR}}^{(\text{night})}$ in \log_{10} (see Equation 4)	Nightside	$\mathcal{U}(-4.0, 3.0)$	$-0.50^{+2.09}_{-2.01}$	$-0.52^{+2.10}_{-2.02}$
H_2O mole fraction in \log_{10}	Nightside	$\mathcal{U}(-12.0, -1.0)$	$-3.13^{+1.33}_{-1.32}$	$-2.42^{+0.69}_{-0.99}$
CO_2 mole fraction in \log_{10}	Nightside	$\mathcal{U}(-12.0, -1.0)$	$-8.80^{+1.64}_{-1.89}$	$-9.02^{+1.92}_{-1.54}$

NOTE—Uncertainties reported here are 1σ . \mathcal{U} is a uniform prior with the lower and upper edges given in parentheses. PC and TR stand for the retrieval on the phase-curve transmission spectrum and the retrieval on the transit-only transmission spectrum, respectively.

2016, 2017; Drummond et al. 2016; Goyal et al. 2018; Sing et al. 2024), a one-dimensional/two-dimensional radiative-convective equilibrium model for planetary atmospheres that has previously been used to interpret WASP-121 b’s emission and transmission spectra observed with HST (Evans et al. 2017, 2018; Mikal-Evans et al. 2020, 2022). The chemical abundances in equilibrium were determined ‘on-the-fly’ by minimizing the Gibbs free energy following the method of Gordon & McBride (1994), and using the thermochemical data from McBride (1993) for 175 neutral, 9 ionic, and 93 condensate species. The molecular opacities of H_2O , CO, and SiO were taken from Barber et al. (2006), Rothman et al. (2010) and Barton et al. (2013), respectively and collision-induced absorption caused by $\text{H}_2\text{-H}_2$ and $\text{H}_2\text{-He}$ collisions was modeled according to Richard et al. (2012). Solar elemental abundances were set from Asplund et al. (2009) and Caffau et al. (2011). The chemistry was fully flexible for any mix of input elemental abundances, and we set the oxygen, carbon and silicon abundances as free parameters relative to the solar abundances in the retrieval along with a scaled solar metallicity parameter for the remaining elements. The

chemistry allowed for the depletion of gas-phase species due to condensation as well as thermal ionization and dissociation. We adopted a ‘Guillot’ P-T profile (Guillot 2010) using two optical channels and one IR channel (Line et al. 2012, 2013) with five fit parameters. The planetary radius is also free to fit along with a gray cloud. A nested sampling statistical algorithm (Feroz & Hobson 2008; Feroz et al. 2009) was used to fit the parameters to the G395H data.

All fit parameters’ posteriors of the fit to both versions of the transmission spectrum are listed in Table 4 and the model’s best fits with the corresponding 1σ intervals are presented in Figure 8 (phase-curve transmission spectrum retrieval) and Figure 15 (transit-only transmission spectrum retrieval) along with the data. For the 349 data points, we found a minimum $\chi^2_{\nu} = 1.32$ in the retrieval on the phase-curve transmission spectrum and a minimum $\chi^2_{\nu} = 1.13$ in the retrieval on the transit-only transmission spectrum. Oxygen and carbon are both constrained to be significantly supersolar in both retrievals, while silicon is found to be supersolar in the retrieval on the phase-curve transmission spectrum, but either subsolar, solar or supersolar in the retrieval on

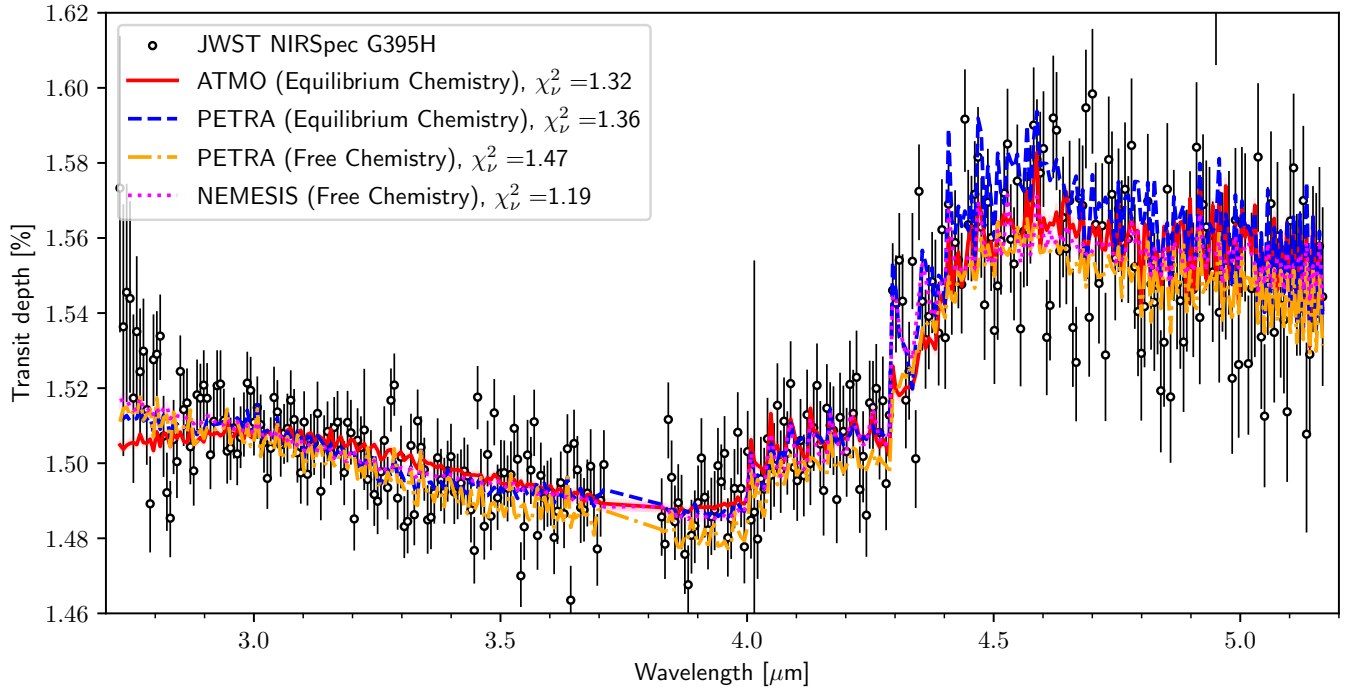


Figure 7. Transmission spectrum at $R \sim 600$ obtained from the phase-curve analysis along with the median model spectra of the applied retrievals. The 1σ intervals of the model spectra are illustrated using shaded regions.

the transit-only transmission spectrum. The P-T profile is inverted in both retrievals with temperatures rising starting at $p \sim 0.1$ bar in the retrieval on the phase-curve transmission spectrum (see Figure 8) and at $p \sim 1$ bar in the retrieval on the transit-only transmission spectrum (see Figure 16). The retrieval on the phase-curve transmission spectrum finds a significantly supersolar C/O of $0.978^{+0.004}_{-0.006}$ (see Figure 10), while the retrieval on the transit-only transmission spectrum finds $0.448^{+0.34}_{-0.26}$ (see Figure 10) which lies close to solar values though both high (0.9) and low (0.1) values are consistent at the 2σ level.

3.3. PETRA (Equilibrium Chemistry)

We used the PETRA retrieval framework (Lothringer & Barman 2020) in a similar setup to ATMO in order to explore the impact of each framework’s model assumptions. PETRA uses the PHOENIX atmosphere model (Hauschildt et al. 1999; Barman et al. 2001) as a forward model in a Differential Evolution Markov Chain (DEMC) statistical framework (Ter Braak 2006; ter Braak & Vrugt 2008). We first performed retrievals with the oxygen-to-hydrogen ratio (O/H) relative to the solar ratio and the C/O as free parameters with chemical abundances governed by chemical equilibrium. Also in line with ATMO, we used the same five-parameter P-T profile parameterization (Guillot 2010; Line et al. 2012, 2013). We also included a free parameter for the refer-

ence radius of the planet and a gray cloud top pressure, below which the atmosphere becomes optically thick at all wavelengths. We took the molecular opacities for H_2O , CO and SiO from Barber et al. (2006), Goorvitch (1994) and Kurucz (1994), respectively, and calculated $\text{H}_2\text{-H}_2$ and He- H_2 collision-induced absorption according to Borysov (1998).

The priors and posteriors of the fit parameters are listed in Table 5 for the retrievals on both data reductions’ transmission spectra and show good agreement between both retrievals within the uncertainties. For the phase-curve transmission spectrum, PETRA returns $\chi^2_\nu = 1.36$ (see Figure 7), while the retrieval on the transit-only transmission spectrum delivers $\chi^2_\nu = 1.01$ (see Figure 16). For both versions of the transmission spectrum, our retrievals find an atmosphere with a sub-solar O/H; however, the results differ for the C/O, which is tightly constrained to be supersolar in the retrieval on the phase-curve transmission spectrum and loosely constrained to be approximately solar to supersolar in the retrieval on the transit-only transmission spectrum (see Figure 10). The temperature profile exhibits a strong inversion beginning at about 10 mbar in both retrievals (see Figure 16), consistent with predictions from self-consistent one-dimensional radiative-convective equilibrium models (Lothringer et al. 2018).

3.4. PETRA (Free Chemistry)

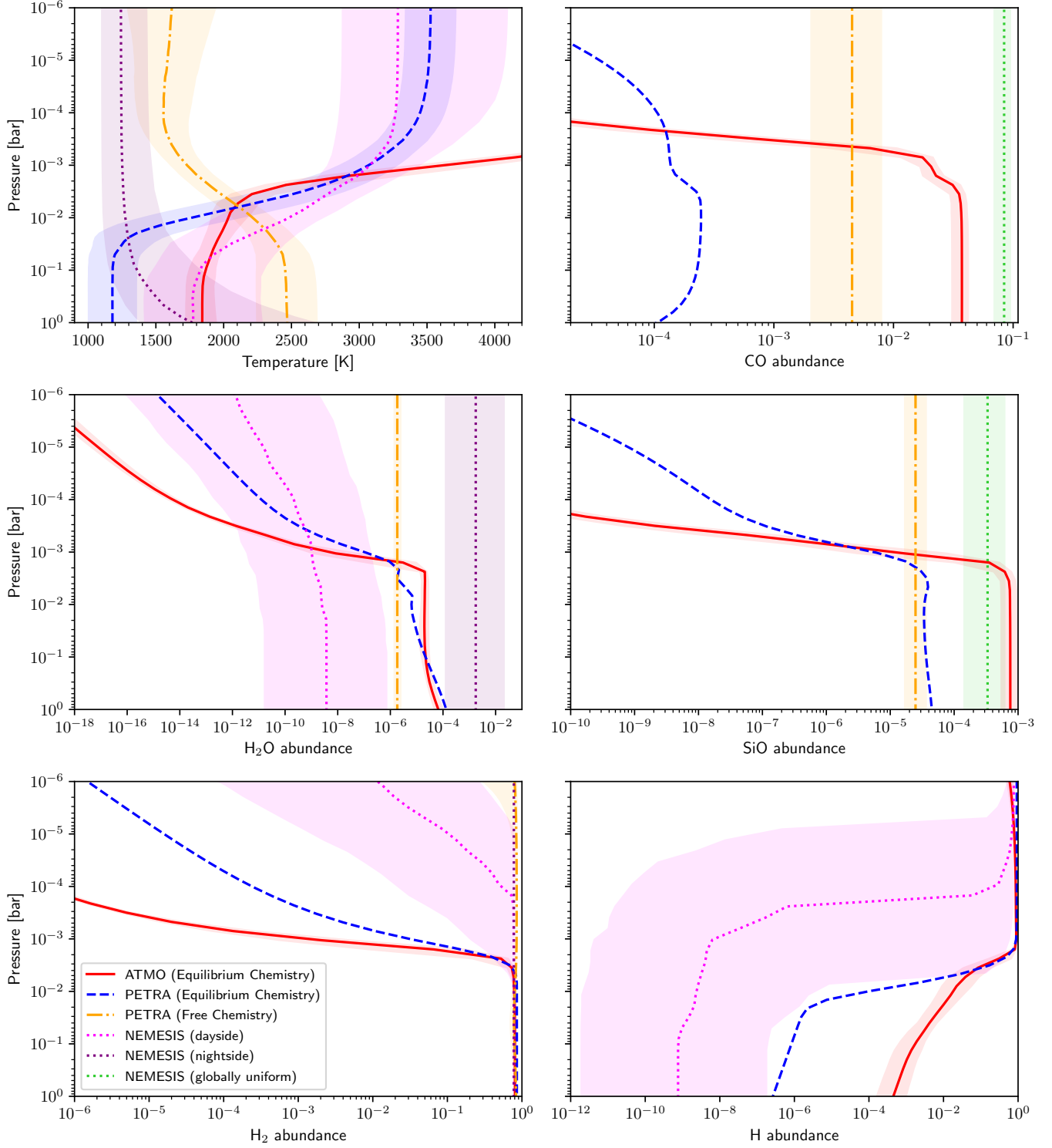


Figure 8. Results from the retrieval frameworks applied to WASP-121 b's transmission spectrum obtained from the phase-curve analysis. The temperature and abundance profiles inferred from the different retrievals are depicted using lines with shaded regions indicating the extent of the corresponding 1σ regions. All NEMESIS results shown here were inferred from a simultaneous retrieval of both hemispheres. Any atmospheric variable varied between the hemispheres in that framework is presented using dotted magenta and purple lines, and the molecular abundances that are held identical in both hemispheres are shown using dotted green lines.

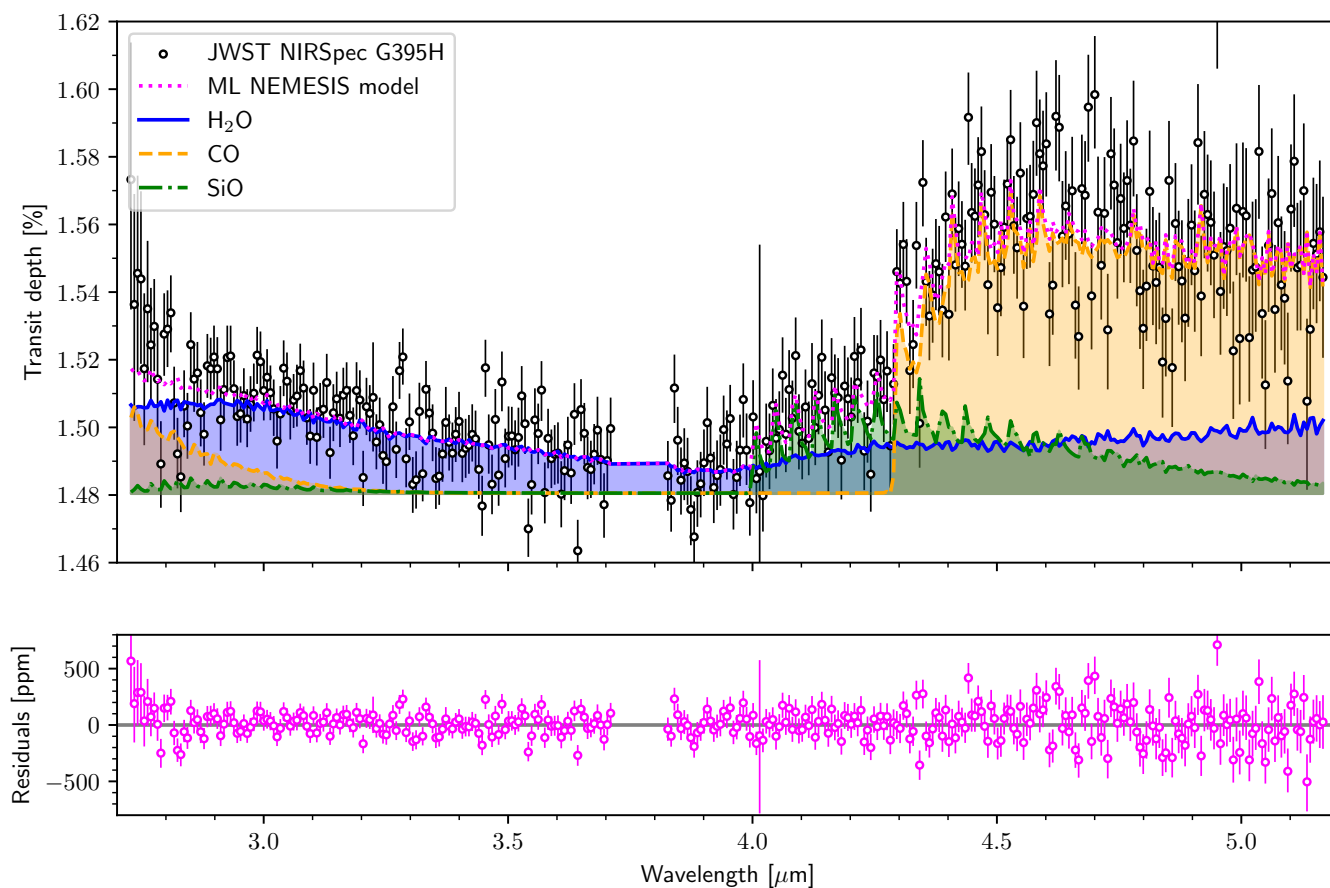


Figure 9. Contributions of the different molecular absorbers to the NEMESIS model spectrum. *Top panel:* the dotted magenta line shows the ML model. The solid blue, dashed orange, and dashed-dotted green lines show model spectra with all molecular opacities except for the opacity due to H₂O, CO and SiO set to zero, respectively. *Bottom panel:* magenta circles depict the data subtracted by the ML NEMESIS model with the data's error bars propagated onto the residuals. A horizontal gray line at zero was added to guide the eye.

Table 4. Inputs and results of the ATMO retrieval.

Parameter	Priors	Posteriors	
		PC	TR
α (see Line et al. 2012, 2013)	$\mathcal{U}(0, 1)$	$0.54^{+0.13}_{-0.07}$	$0.41^{+0.17}_{-0.22}$
β (see Line et al. 2012, 2013)	$\mathcal{U}(0, 1)$	$0.84^{+0.02}_{-0.03}$	$0.88^{+0.06}_{-0.08}$
κ_{IR} in \log_{10} (see Guillot 2010; Line et al. 2012, 2013)	$\mathcal{U}(-4.0, 0.5)$	$-2.45^{+0.06}_{-0.07}$	$-3.18^{+0.34}_{-0.45}$
γ_1 in \log_{10} (see Guillot 2010; Line et al. 2012, 2013)	$\mathcal{U}(-0.5, 3.5)$	$0.39^{+0.40}_{-0.38}$	$0.92^{+0.25}_{-0.22}$
γ_2 in \log_{10} (see Guillot 2010; Line et al. 2012, 2013)	$\mathcal{U}(-1.5, 3.5)$	$2.57^{+0.07}_{-0.12}$	$0.25^{+0.57}_{-0.63}$
Grey cloud deck pressure in ln	$\mathcal{U}(-10, 10)$	$-3.16^{+0.66}_{-0.33}$	$-1.22^{+1.26}_{-1.51}$
WASP-121 b’s radius relative to Jupiter’s radius	$\mathcal{U}(1.69, 1.9)$	$1.79^{+0.00}_{-0.00}$	$1.76^{+0.01}_{-0.01}$
Elemental abundances other than H, He, C, O, and Si relative to solar in \log_{10}	$\mathcal{U}(-2.8, 2.8)$	$-0.65^{+0.15}_{-0.14}$	$0.24^{+0.88}_{-1.10}$
Carbon abundance relative to solar abundance in \log_{10}	$\mathcal{U}(-1, 2)$	$1.86^{+0.06}_{-0.08}$	$1.37^{+0.19}_{-0.19}$
Oxygen abundance relative to solar abundance in \log_{10}	$\mathcal{U}(-1, 2)$	$1.16^{+0.06}_{-0.08}$	$1.46^{+0.25}_{-0.15}$
Silicon abundance relative to solar abundance in \log_{10}	$\mathcal{U}(-1, 2)$	$1.17^{+0.11}_{-0.14}$	$0.45^{+0.31}_{-0.52}$

NOTE—Uncertainties reported here are 1σ . \mathcal{U} is a uniform prior with the lower and upper edges given in parentheses. PC and TR stand for the retrieval on the phase-curve transmission spectrum and the retrieval on the transit-only transmission spectrum, respectively.

Table 5. Results of the PETRA retrieval prescribing chemical equilibrium in the atmosphere.

Parameter	Priors	Posteriors	
		PC	TR
α (see Line et al. 2012, 2013)	$\mathcal{U}(0, 1)$	$0.44^{+0.31}_{-0.26}$	$0.40^{+0.26}_{-0.24}$
β (see Line et al. 2012, 2013)	$\mathcal{U}(0.3, 1.4)$	$0.60^{+0.08}_{-0.08}$	$0.64^{+0.22}_{-0.16}$
γ_1 in \log_{10} (see Guillot 2010; Line et al. 2012, 2013)	$\mathcal{U}(-2, 4)$	$1.92^{+0.31}_{-0.28}$	$1.95^{+0.67}_{-0.65}$
γ_2 in \log_{10} (see Guillot 2010; Line et al. 2012, 2013)	$\mathcal{U}(-2, 4)$	$1.86^{+0.34}_{-0.32}$	$0.88^{+1.08}_{-0.81}$
κ_{IR} in \log_{10} (see Guillot 2010; Line et al. 2012, 2013)	$\mathcal{U}(-4, 1.5)$	$-2.73^{+0.27}_{-0.30}$	$-2.50^{+0.51}_{-0.57}$
Cloud top pressure (\log_{10} barye)	$\mathcal{U}(-3, 10)$	$5.93^{+1.44}_{-0.67}$	$7.38^{+1.57}_{-1.34}$
WASP-121 b’s radius in 10^{10} cm	$\mathcal{U}(0.1, 2.5)$	$1.195^{+0.004}_{-0.005}$	$1.183^{+0.007}_{-0.009}$
O/H relative to solar in \log_{10}	$\mathcal{U}(-2.5, 1.0)$	$-0.60^{+0.17}_{-0.15}$	$-0.48^{+0.36}_{-0.23}$
C/O	$\mathcal{U}(0.001, 100)$	$0.80^{+0.06}_{-0.06}$	$0.59^{+0.13}_{-0.12}$

NOTE—Uncertainties reported here are 1σ . \mathcal{U} is a uniform prior with the lower and upper edges given in parentheses. PC and TR stand for the retrieval on the phase-curve transmission spectrum and the retrieval on the transit-only transmission spectrum, respectively.

To test how sensitive our interpretation of the data is to the assumption of chemical equilibrium, we also ran PETRA in a “free chemistry” setup, where the abundances of important molecular absorbers are allowed to vary as free parameters. In this free chemistry framework, we fit for the abundances of H_2O , CO and SiO with pressure-independent abundances. This allows the retrieval to fit atmospheric compositions that may deviate from chemical equilibrium, but introduces other assumptions such as a lack of thermal dissociation of these species. In contrast, the H_2 and H abundances were set according to chemical equilibrium to include the impact of H_2 dissociation without introducing additional fit parameters. We adopted the same five-parameter P-T profile, cloud parameterization, opacity information, and fit method-

ology of the PETRA retrieval enforcing chemical equilibrium (see Section 3.3).

The posteriors of the retrievals’ fit parameters are listed in Table 6 and agree well between the retrievals on both transmission spectra, except for the P-T profile parameters, which lead to fundamentally different P-T profiles (see Figures 8 and 16). The retrieval on the phase-curve transmission spectrum finds temperatures that generally decrease with height, while the retrieval on the transit-only transmission spectrum results in an inverted temperature structure. The inversion is of similar magnitude and temperature to the PETRA chemical equilibrium retrieval, but occurs at a lower pressure (~ 1 mbar).

Table 6. Inputs and results for the PETRA retrieval employing free chemical abundances.

Parameter	Prior	Posteriors	
		PC	TR
α (see Line et al. 2012, 2013)	$\mathcal{U}(0, 1)$	$0.80^{+0.14}_{-0.19}$	$0.41^{+0.27}_{-0.23}$
β (see Line et al. 2012, 2013)	$\mathcal{U}(0.25, 1.75)$	$0.72^{+0.09}_{-0.09}$	$0.84^{+0.12}_{-0.12}$
γ_1 in \log_{10} (see Guillot 2010; Line et al. 2012, 2013)	$\mathcal{U}(-2, 4)$	$0.26^{+0.68}_{-0.63}$	$1.47^{+0.67}_{-0.65}$
γ_2 in \log_{10} (see Guillot 2010; Line et al. 2012, 2013)	$\mathcal{U}(-2, 4)$	$-0.99^{+0.34}_{-0.36}$	$0.50^{+1.18}_{-1.05}$
κ_{IR} in \log_{10} (see Guillot 2010; Line et al. 2012, 2013)	$\mathcal{U}(-4, 1.5)$	$-0.17^{+0.48}_{-0.53}$	$-0.63^{+0.55}_{-0.74}$
Cloud top pressure (\log_{10} Ba)	$\mathcal{U}(-3, 15)$	$10.02^{+2.85}_{-2.94}$	$4.26^{+0.48}_{-0.43}$
WASP-121 b’s radius in 10^{10} cm	$\mathcal{U}(0.1, 2.5)$	$1.231^{+0.008}_{-0.009}$	$1.218^{+0.006}_{-0.006}$
H ₂ O mole fraction in \log_{10}	$\mathcal{U}(-15, -2)$	$-5.74^{+0.12}_{-0.11}$	$-4.95^{+0.58}_{-0.46}$
CO mole fraction in \log_{10}	$\mathcal{U}(-15, -2)$	$-2.34^{+0.24}_{-0.34}$	$-2.90^{+0.59}_{-0.67}$
SiO mole fraction in \log_{10}	$\mathcal{U}(-15, -2)$	$-4.60^{+0.16}_{-0.17}$	$-3.87^{+0.62}_{-0.52}$

NOTE—Uncertainties reported here are 1σ . \mathcal{U} is a uniform prior with the lower and upper edges given in parentheses. PC and TR stand for the retrieval on the phase-curve transmission spectrum and the retrieval on the transit-only transmission spectrum, respectively.

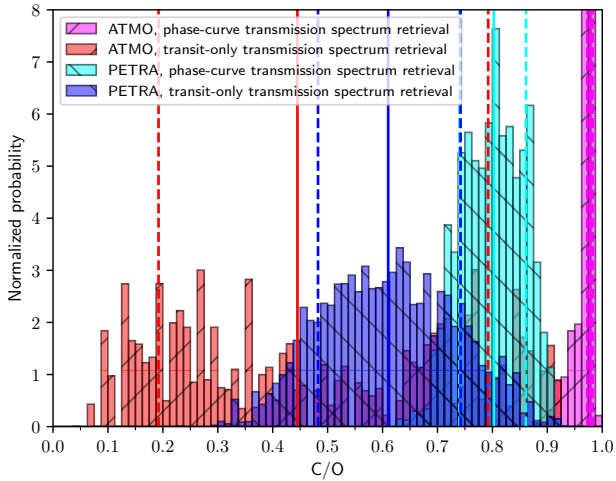


Figure 10. Posteriors for WASP-121 b’s C/O inferred from the retrievals enforcing equilibrium chemistry. The solid vertical lines depict the posteriors’ medians and the dashed vertical lines show the edges of the 1σ intervals. Two bars of the posteriors of the ATMO retrieval on the phase-curve transmission spectrum exceed the y-axis: their normalized probability values are ~ 14.5 and ~ 59.2 from left to right.

The phase-curve transmission spectrum is fit with a $\chi^2_{\nu} = 1.47$ and the fit to the transit-only transmission spectrum results in $\chi^2_{\nu} = 1.20$. In both retrievals, the CO abundance posterior is limited by running up against the upper edge of the uniform prior at 1.0×10^{-2} (see Table 6), which might have an impact on the goodness of fit. In the retrievals on both versions of the transmission spectrum, the H₂O and SiO abundances are generally consistent with the PETRA retrievals prescribing chemical equilibrium; however, the CO abundances of the free chemistry retrievals are both higher than those in the

chemical equilibrium retrievals (see Figures 8 and 16). To test whether including SiO in the model is justified, we also ran the same free chemistry retrieval setup without SiO and calculated the Bayesian information criterion (BIC) between the two different models for both the retrieval on the phase-curve transmission spectrum and the retrieval on the transit-only transmission spectrum. This resulted in a $\Delta\text{BIC} = 2.0$ in the retrieval on the phase-curve transmission spectrum and a $\Delta\text{BIC} = 8.9$ in the retrieval on the transit-only transmission spectrum in favor of the model including SiO.

3.5. GCM comparison

WASP-121 b’s atmosphere is expected to be extremely inhomogeneous due to the drastic differences in temperatures, and thus the thermal dissociation, between the dayside and the nightside (see Section 1). As these effects are intrinsically three-dimensional, GCMs can yield important insight into the physics of the atmosphere when comparing their simulated transmission spectra to observations.

Figure 11 shows WASP-121 b’s transmission spectrum derived from the phase-curve analysis of the NIRSpc G395H observation together with model spectra derived by Pluriel et al. (2020) from the GCM of Parmentier et al. (2018). The GCM of Parmentier et al. (2018) did not include the effects of thermal dissociation on the atmosphere’s mean molecular weight and latent heat, so Pluriel et al. (2020) postprocessed the effect of H₂O and H₂ dissociation onto the GCM output to demonstrate its impact on the transmission spectrum. When no dissociation is taken into account (blue dotted line), the model spectrum poorly represents the data, since the slope of the H₂O feature on the NRS1 detector is too steep and the amplitude of the CO feature on the NRS2 detec-

tor is too small. Including H₂O dissociation (orange dashed line) flattens the slope of the H₂O feature, since the dissociation reduces the H₂O abundance on the dayside. The resulting absorption band thus originates from the nightside which creates smaller variations in transit depth due to its lower temperatures and higher mean molecular weight compared to the dayside. Further incorporating H₂ dissociation into the model (red solid line) mostly acts to increase the amplitude of the CO absorption band, because the resulting decrease in mean molecular weight inflates the atmospheric scale height of the dayside, leading to an increase in the strength of the absorption features of any molecule that is present on the dayside. As CO, unlike H₂O, is abundant on the dayside, including H₂ dissociation changes the observed CO band, but not the H₂O band.

Pluriel et al. (2020)’s model spectra only include CO and H₂O, but not SiO opacities, leading to a substantial underestimation of the transit depth between 4.0 μm and 4.3 μm in all models. However, it is notable that the agreement between the data and models progressively improves as more realistic three-dimensional effects, namely the effects of the thermal dissociation of H₂O and H₂ on the mean molecular weight and latent heat of the atmosphere, are added.

4. DISCUSSION

4.1. Thermal dissociation

Thermal dissociation and molecular recombination strongly depend on temperature, and thus, in a tidally locked planet such as WASP-121 b, they are variable in latitude, longitude, and altitude (see, e.g., Bell & Cowan 2018; Parmentier et al. 2018). Fully grasping their effects on the transmission spectrum thus requires a three-dimensional model. The GCM simulations presented by Pluriel et al. (2020) showcase the importance of both H₂ and H₂O dissociation on WASP-121 b’s dayside as including H₂O dissociation is needed to fit the slope of the transmission spectrum between 2.7 and 3.7 μm and the dissociation of H₂ inflates the CO absorption feature at wavelengths longer than 4.3 μm to the observed levels (see Figure 11). These findings suggest that including changes of the mean molecular weight and latent heat induced by thermal dissociation in the model leads to a more accurate representation of the planet’s atmospheric physics.

The role of thermal dissociation in our NEMESIS, ATMO and PETRA models that are all not fully three-dimensional is less evident. NEMESIS is our only model that is capable of grasping the thermochemical differences between the two hemispheres of WASP-121 b as we divided the ray across the atmosphere into dayside

and nightside integrals and fit for different thermochemical conditions in both hemispheres. Our NEMESIS retrievals favor a decrease of both the H₂ and H₂O abundances in the upper dayside atmosphere (see Figures 8 and 16) as well as a higher H₂O abundance on the nightside than on the dayside in the lower atmosphere ($p \gtrsim 0.1$ bar) consistent with thermal dissociation. However, the decreases with height of both the H₂ abundance ($\alpha_{\text{H}_2} = 0.97^{+0.61}_{-0.61}$ and $\alpha_{\text{H}_2} = 0.92^{+0.58}_{-0.57}$ in the retrievals on the phase-curve and transit-only transmission spectra, respectively) and the H₂O abundance ($\alpha_{\text{H}_2\text{O}} = 1.45^{+0.91}_{-0.89}$ and $\alpha_{\text{H}_2\text{O}} = 1.60^{+0.84}_{-0.93}$ in the retrievals on the phase-curve and transit-only transmission spectra, respectively) are consistent with zero within 2σ . The differences between the deep atmospheric water abundances of the dayside ($-8.44^{+2.29}_{-2.21}$ and $-7.83^{+2.63}_{-2.49}$ in the retrievals on the phase-curve and transit-only transmission spectra, respectively) and the nightside ($-3.13^{+1.33}_{-1.32}$ and $-2.42^{+0.69}_{-0.99}$ in the retrievals on the phase-curve and transit-only transmission spectra, respectively) are 2.0σ in the retrieval on the phase-curve transmission spectrum and 1.9σ in the retrieval on the transit-only transmission spectrum. Thus, these differences are also not significantly different from zero. However, a lower dayside H₂O abundance compared to the nightside is in agreement with GCM simulations (Parmentier et al. 2018), suggesting that the different H₂O abundances between the hemispheres in our retrievals might be driven by thermal dissociation. Similar to our results, recent Gemini-S/IGRINS observations of WASP-121 b suggest a higher H₂O abundance on the dayside than on the nightside (Wardenier et al. 2024) and its phase-curve observed using HST (Mikal-Evans et al. 2022) points toward a difference of many orders of magnitude in the dayside and nightside H₂O abundances in the part of the atmosphere that is typically observed in transmission spectroscopy ($p \sim 10^{-3}$ bar). Mikal-Evans et al. (2022) inferred very similar dayside and nightside H₂O abundances in the lower atmosphere ($p \gtrsim 10^{-2}$ bar); however, as observations of thermal emission of hot Jupiters are generally sensitive to higher pressure-ranges compared to transit observations, that part of the atmosphere is probably unconstrained by our analysis of WASP-121 b’s transmission spectrum.

The decrease of the quality of fit when moving from a chemical equilibrium model including thermal dissociation to one with free chemistry but with pressure-independent abundances and thus no thermal dissociation within the PETRA retrieval framework might be a potential hint toward the importance of thermal dissociation. Despite having one more free parameter, the retrievals with free chemistry deliver $\chi^2_{\nu} = 1.47$ for the

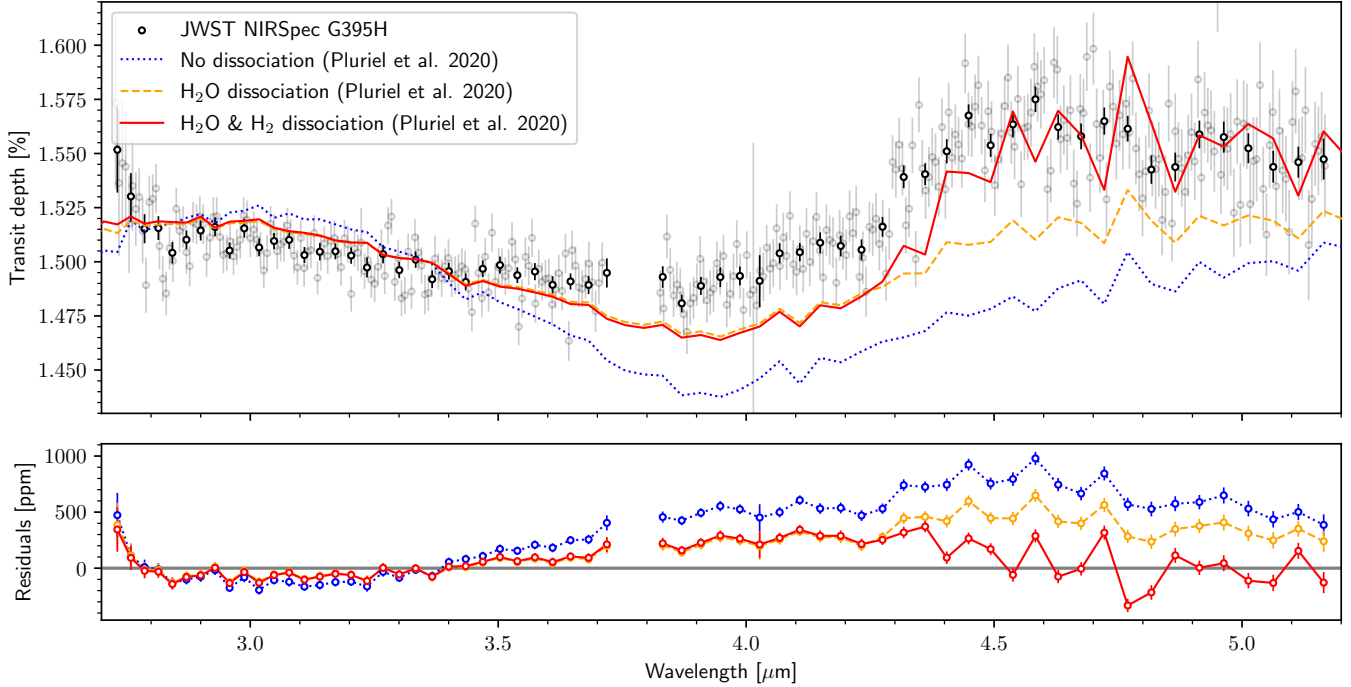


Figure 11. WASP-121 b’s transmission spectrum obtained from the phase-curve analysis at a spectral resolution of $R \sim 600$ and the GCM transmission spectra presented by [Pluriel et al. \(2020\)](#). *Upper panel:* the gray circles show the original data and the black circles show the data binned in wavelength. The model spectra presented by [Pluriel et al. \(2020\)](#) with varying degrees of molecular dissociation are plotted using lines. A wavelength-independent offset was added to the model spectra to fit the mean of the data between $2.9 \mu\text{m}$ and $3.7 \mu\text{m}$. *Lower panel:* the residuals between the model spectra with an added constant and the data are depicted using colored circles with the error bars of the data propagated onto the residuals. A horizontal gray line at zero was added to guide the eye.

phase-curve transmission spectrum and $\chi_\nu^2 = 1.20$ for the transit-only transmission spectrum, while the retrievals enforcing chemical equilibrium return $\chi_\nu^2 = 1.36$ for the phase-curve transmission spectrum and $\chi_\nu^2 = 1.01$ for the transit-only transmission spectrum. However, these differences in χ_ν^2 are not conclusive evidence for thermal dissociation and might also be caused by the free chemistry retrievals being limited by running into the upper edge of the uniform prior on the CO abundance (see Section 3.4).

4.2. Molecular abundances

Dichotomies between different molecules’ global distributions probably leave an impact on transmission spectra (see Section 1). The much higher temperatures on the dayside, compounded by the dissociation of H_2 into atomic hydrogen, act to increase the scale height over that on the nightside, leading to an inflation of the absorption features of any molecule that is abundant on the dayside, such as CO (see Figure 11). This potentially gives rise to a negative correlation between the amount of H_2 dissociation and the CO abundances inferred from atmospheric models.

We potentially observe this degeneracy in our atmospheric models. The NEMESIS model, which finds the highest CO abundance among our models, also finds less H_2 dissociation than the ATMO and PETRA equilibrium chemistry models, since NEMESIS’s H_2 abundances are higher in all parts of the atmosphere than the other two models’ H_2 abundances (see Figures 8 and 16). Therefore, the CO abundance inferred using NEMESIS might be partly driven by less H_2 dissociation. The only models that find less H_2 dissociation than NEMESIS are the free chemistry PETRA retrievals. However, the CO abundance posteriors of these retrievals are limited by the upper edge of the adopted uniform prior at 1% (see Table 6), which prevents the posterior from reaching similar CO levels to those of the NEMESIS retrieval. Within the PETRA framework, the CO abundance of the free chemistry retrieval, which includes less H_2 dissociation than the chemical equilibrium model, is higher than the chemical equilibrium model’s CO abundance. Thus, the PETRA retrievals follow the trend of including higher CO abundances with less H_2 dissociation. ATMO finds lower CO abundances than NEMESIS, but higher CO abundances than PETRA. However, in the retrieval on the phase-curve transmission spectrum (Figure 8), the ATMO

model reaches temperatures high enough to dissociate CO, which probably complicates the picture between H₂ dissociation and CO abundances. Therefore, all CO abundances we inferred from the different atmospheric models might be biased and we cannot derive a quantitative constraint.

The H₂O abundances we derived using ATMO and PETRA agree around 0.1 – 1 mbar (see Figures 8 and 16), the part of the atmosphere that is typically observed in transmission spectroscopy. The dayside and nightside H₂O abundance profiles from NEMESIS deliver lower and higher abundances, respectively, than the other models’ abundance profiles in the observable part of the atmosphere. Thus, the inferred abundances are to first order compatible with dissociation on the dayside and with recombination on the nightside. This demonstrates that modeling the thermochemical conditions of both hemispheres is crucial for constraining the planet’s bulk H₂O content as the bulk inventory is approximated more closely by the nightside abundance that is not modified by dissociation.

For SiO, our models find consistent abundances when retrieving on the transit-only transmission spectrum (see Figure 16) and abundances spanning from $\sim 2 \times 10^{-5}$ to $\sim 10^{-3}$ when fitting the phase-curve transmission spectrum (see Figure 8). Our ATMO and PETRA retrievals enforcing equilibrium chemistry suggest that SiO is more susceptible to thermal dissociation than CO, but more stable against it than H₂O, as the decrease of its abundances starts at lower pressures and follows smaller gradients (see Figures 8 and 16). Thus, the degree to which the SiO abundances are impacted by a degeneracy with H₂ dissociation and the degree of reliability of our inferred abundances remain unclear. However, the fact that both ATMO and PETRA find observable amounts of SiO in equilibrium chemistry delivers a direct explanation for SiO in WASP-121 b: SiO is a molecule whose observable presence in WASP-121 b does not require disequilibrium processes such as photochemistry or mixing from deeper levels of the atmosphere.

4.3. Elemental abundance ratios

The constraints on WASP-121 b’s C/O we inferred using ATMO and PETRA are informed by absorption from CO, SiO, and H₂O. As these molecules are susceptible to thermal dissociation in different degrees (see Section 4.2), the three-dimensional nature of dissociation probably biases the results of this elemental abundance ratio (Pluriel et al. 2020).

Both ATMO and PETRA prescribing chemical equilibrium constrain WASP-121 b’s C/O to be significantly supersolar in their respective retrievals on the phase-

curve transmission spectrum ($0.978^{+0.004}_{-0.006}$ in ATMO and $0.80^{+0.06}_{-0.06}$ in PETRA; see Figure 10). In the retrievals on the transit-only transmission spectrum, PETRA favors a solar to supersolar C/O ($0.59^{+0.13}_{-0.12}$), while ATMO finds solutions compatible with both a supersolar and a subsolar C/O ($0.45^{+0.34}_{-0.26}$). Therefore, our retrievals appear to overall favor WASP-121 b to have a supersolar C/O. However, given the challenges in deriving the abundances of molecules whose absorption features are sensitive to the different hemispheres of the planet when applying one-dimensional models (Pluriel et al. 2020) and the fact that our results span C/O = 0.19 to C/O = 0.98 in the retrieval posteriors’ 1 σ intervals, we cannot derive a quantitative constraint. Other elemental ratios such as refractory-to-volatile ratios (e.g., Si/C or Si/O) would also rely on the relative absorption strengths of SiO, CO, and H₂O. Thus, these ratios are probably susceptible to biases similar to the ones affecting C/O and we refrain from attempting to constrain them.

4.4. Identification of absorbers

The challenges in constraining the abundances of absorbing molecules and elemental abundance ratios in WASP-121 b described above do not affect our ability to identify the molecules responsible for the observed atmospheric absorption (see, e.g., Jaziri et al. 2024). What drives the detection significances of molecules in the atmosphere is the model’s fit to the observed transmission spectrum, which depends on the shape of the molecules’ absorption features in wavelength. As these absorption features’ shapes do not change significantly when moving to more complex atmospheric models, it is unlikely that any absorber’s detection would disappear when moving to a more complex atmospheric model.

Since the shape of the transmission spectrum is matched closely by the H₂O and CO opacities in both our models (see Figure 9) and the models presented by Pluriel et al. (2020) that only include CO and H₂O opacities (Figure 11), both molecules’ contributions to the transmission spectrum are evident. Notably, there is a clear underestimation of atmospheric absorption in the model spectra presented by Pluriel et al. (2020) between $\lambda \sim 4.0$ and $\lambda \sim 4.3 \mu\text{m}$ (see Figure 11), hinting at the existence of at least one more absorber in addition to H₂O and CO. In our NEMESIS model, the dominant absorber in that wavelength range is SiO, which contributes more opacity than both H₂O and CO (see Figure 9). To quantify the statistical significance of SiO in these observations, we performed retrievals excluding SiO from the atmosphere in NEMESIS and PETRA, both allowing free chemistry. Comparing the Bayesian

evidence of the NEMESIS retrievals delivers a conclusive detection significance of 5.2σ in favor of including SiO in the model in the retrieval on the phase-curve transmission spectrum and a tentative detection of 2.4σ in the retrieval on the transit-only transmission spectrum. When going from the SiO-less model to the one including SiO in PETRA modeling free chemical abundances, the changes in the BIC are 2.0 and 8.9 in the retrieval on the phase-curve transmission spectrum and the retrieval on the transit-only transmission spectrum, respectively, delivering moderate and strong evidence in favor of including SiO. As the phase-curve transmission spectrum has been shown to be more precise than the transit-only transmission spectrum thanks to the inclusion of all observations in the data analysis (see Section 2.2), we consider inferences from the former data reduction more reliable. The NEMESIS framework appears to be the most reliable retrieval for WASP-121 b’s transmission spectrum, as its results agree the most between the retrievals on both versions of the transmission spectrum (see Tables 3, 4, 5, and 6), as it allows for the expected heterogeneity between WASP-121 b’s dayside and nightside and as it delivers the lowest χ^2_ν values for both versions of the transmission spectrum. Additionally, and unlike PETRA, it directly calculates the Bayesian evidence. Thus, we consider the detection significance of 5.2σ found in the NEMESIS retrieval on the phase-curve transmission spectrum the most reliable one.

SiO is a molecule consistent with chemical equilibrium in WASP-121 b (see Section 4.2), providing a direct explanation of its presence in observable abundances. Additionally, it has previously been suggested as a source of the observed NUV opacity in WASP-121 b and WASP-178 b (Lothringer et al. 2020, 2022). Our detection of SiO is thus in line with its previously hypothesized impact on WASP-121 b’s NUV transmission spectrum.

4.5. Light-curve systematics

The fit to the white light curves (see Figure 1) delivers a χ^2_ν of 1.42 for the simultaneous fit. The spectrophotometric light-curve fits at both presented spectral resolutions appear to be effectively free of systematic residuals (see Figure 3) and the χ^2_ν of the fits to the $R \sim 600$ light curves are mostly close to 1 (see Figure 13).

However, there is one apparent feature in the residuals of the fit to the white light curve of NRS2 that is absent in the fit to the white light curve of NRS1. This feature is a collection of negative residuals between $\text{BJD}_{\text{TDB}} = 2459867.6632$ and $\text{BJD}_{\text{TDB}} = 2459867.6894$, just before egress starts (see Figure 1, the dashed line in the lower panel of Figure 2 and Mikal-Evans et al. 2023). As these residuals are not symmetric about the transit

midtime, they are most likely explained by instrumental or stellar systematics or deviations of the planet’s shape from a sphere. Recent studies of transit signals of exoplanets with asymmetric terminators have shown, however, that limb asymmetries mostly affect the transit signal during ingress and egress (see, e.g., Espinoza & Jones 2021; Grant & Wakeford 2023). Indeed, the unexplained residuals are also apparent in our *catwoman* fits to the white light curves (see Figure 14). Thus, it is unlikely that these residuals we observe are caused by asymmetric limbs. Alternatively, the different sizes of the planet’s dayside and nightside might create the unexplained residuals before egress in the NRS2 light curve (Falco et al. 2024). Possibly, only the NRS2 but not the NRS1 light curve is sensitive to the different extents of the two hemispheres, because both H₂O and CO absorb in NRS2’s bandpass, while the NRS1 bandpass is mostly sensitive to H₂O (see Figure 9). Thus, the dayside is effectively transparent in the NRS1 light curve, but absorbing in the NRS2 light curve, making the NRS1 light curve sensitive to the nightside only, while the NRS2 light curve probes both the dayside and nightside.

As none of the identified residuals are apparent in each individual spectrophotometric light-curve fit (see Figure 2), we are confident that these residuals do not leave a significant impact on the extracted transmission spectrum. However, modeling the impact of the dayside and nightside on the white light curves might be a promising path toward understanding the unexplained residuals in our NRS2 white light curve fit.

5. SUMMARY AND CONCLUSIONS

The JWST observations of a full phase-curve of the ultrahot Jupiter WASP-121 b using NIRSpec G395H have delivered an observation of the planet’s transmission spectrum between $\sim 2.7 \mu\text{m}$ and $\sim 5.2 \mu\text{m}$ of unprecedented quality. Analyzing the planet’s full phase-curve instead of a cutout of the transit from the observations appears to reduce the contamination of the inferred transmission spectrum with the planet’s nightside emission significantly. Additionally, the full phase-curve analysis delivers a more precise transmission spectrum with $\sim 40\%$ smaller error bars due to stronger constraints on the phase-curve shape, which is correlated with the transit depth. Both the white and spectrophotometric light curves show no evidence for asymmetric limbs in WASP-121 b, allowing an analysis of the transmission spectrum without modeling differences between the planet’s morning and evening terminators.

H₂O and CO are apparent in the transmission spectrum, with evidence for the existence of at least one more molecule absorbing stellar radiation between $\lambda \sim 4.0 \mu\text{m}$

and $\lambda \sim 4.3 \mu\text{m}$. From our NEMESIS retrievals, we identify that absorber as SiO at a statistical significance of 5.2σ . Comparative retrievals within the ATMO and PETRA frameworks that enforce chemical equilibrium show that the observed SiO feature is compatible with equilibrium chemistry in the atmosphere. Thus, not only does SiO fit the observed spectral feature, its presence in WASP-121 b at observable quantities also does not require disequilibrium chemistry.

Previous modeling efforts simulating WASP-121 b's transmission spectrum using a GCM have shown that changes in the mean molecular weight and latent heat induced by thermal dissociation of H₂O and H₂ modify the shapes of the absorption features of H₂O and CO (Pluriel et al. 2020). Our JWST/NIRSpec G395H observations are approximated best when including both H₂O and H₂ dissociation, demonstrating the importance of thermal dissociation when deriving the transmission spectrum from the planet's three-dimensional shape. As CO is more stable against thermal dissociation than H₂O, the observed CO feature is sensitive to H₂ dissociation on the dayside, while the H₂O feature is not. Therefore, quantitative constraints on these molecules' abundances require an adequate representation of the thermochemical heterogeneity between WASP-121 b's dayside and nightside. We attempted to model this heterogeneity using the NEMESIS framework by splitting the ray through the atmosphere into dayside and nightside integrals. The atmospheric model inferred from the NEMESIS retrieval fits the observations well, but does not deliver a statistically significant improvement over a comparatively simpler model without hemispheric differences. However, the retrieval allowing chemical differences between the two hemispheres finds a higher H₂O abundance on the nightside than on the dayside, demonstrating the impact of hemispheric heterogeneity when attempting to constrain the planet's bulk H₂O inventory. From the comparison of model findings within the NEMESIS, ATMO and PETRA frameworks, we conclude that molecular abundances and elemental abundance ratios are prone to biases and degeneracies that might be caused by a negative correlation between H₂ dissociation and CO abundances. These issues, which stem from the three-dimensional nature of the planet, prevent us from constraining molecular abundances and elemental abundance ratios from the observed transmission spectrum with the analyses we present here.

Constraining the abundance of SiO in WASP-121 b as well as the abundances of H₂O and CO would open up

new observables of the planet's chemical inventory, such as refractory-to-volatile ratios. These ratios would inform us about the amount of rocky material accreted by the planet during its formation and thus help to constrain its migration history. However, as the molecules needed to establish a picture of WASP-121 b's elemental abundance ratios differ in their stabilities against thermal dissociation, any quantitative constraints require a careful representation of the three-dimensional effects of dissociation in the applied atmospheric model.

1 This work is based on observations made with the
 2 NASA/ESA/CSA James Webb Space Telescope. The
 3 data were obtained from the Mikulski Archive for Space
 4 Telescopes at the Space Telescope Science Institute,
 5 which is operated by the Association of Universities for
 6 Research in Astronomy, Inc., under NASA contract NAS
 7 5-03127 for JWST. The specific observations analyzed
 8 can be accessed via DOI: [10.17909/6qnn-6j23](https://doi.org/10.17909/6qnn-6j23). C.G.
 9 and T.M.E.-S. thank J r my Leconte and Tiziano Zin-
 10 gales for fruitful discussions and for providing the sim-
 11 ulated transmission spectra published in Pluriel et al.
 12 (2020) and plotted in Figure 11 in machine-readable
 13 format. J.K.B. is supported by a Science and Tech-
 14 nology Facilities Council Ernest Rutherford Fellowship
 15 [ST/T004479/1]. N.J.M. acknowledges support from
 16 a UKRI Future Leaders Fellowship [MR/T040866/1],
 17 a Science and Technology Facilities Council Consoli-
 18 dated Grant [ST/R000395/1] and the Leverhulme Trust
 19 through a research project grant [RPG-2020-82].

Facilities: JWST.

Software: `astropy` (Astropy Collaboration et al. 2013, 2018, 2022), `ATMO` (Amundsen et al. 2014; Tremblin et al. 2015, 2016, 2017; Drummond et al. 2016; Goyal et al. 2018), `batman` (Kreidberg 2015), `catwoman` (Espinoza & Jones 2021; Jones & Espinoza 2022), `corner` (Foreman-Mackey 2016), `dynesty` (Speagle 2020), `emcee` (Foreman-Mackey et al. 2013), `ExoTIC-LD` (Grant & Wakeford 2022), `FIREFLY` (Rustamkulov et al. 2022, 2023), `lmfit` (Newville et al. 2015), `matplotlib` (Hunter 2007), `MultiNest` (Feroz et al. 2009; Feroz et al. 2019), `NEMESIS` (Irwin et al. 2008; Lee et al. 2012), `numpy` (Harris et al. 2020), `pandas` (McKinney 2010), `PETRA` (Lothringer & Barman 2020), `PyMultiNest` (Buchner et al. 2014), `scipy` (Virtanen et al. 2020).

REFERENCES

- Amundsen, D. S., Baraffe, I., Tremblin, P., et al. 2014, *A&A*, 564, A59, doi: [10.1051/0004-6361/201323169](https://doi.org/10.1051/0004-6361/201323169)
- Asplund, M., Grevesse, N., Sauval, A. J., & Scott, P. 2009, *ARA&A*, 47, 481, doi: [10.1146/annurev.astro.46.060407.145222](https://doi.org/10.1146/annurev.astro.46.060407.145222)

- Astropy Collaboration, Robitaille, T. P., Tollerud, E. J., et al. 2013, *A&A*, 558, A33, doi: [10.1051/0004-6361/201322068](https://doi.org/10.1051/0004-6361/201322068)
- Astropy Collaboration, Price-Whelan, A. M., Sipőcz, B. M., et al. 2018, *AJ*, 156, 123, doi: [10.3847/1538-3881/aabc4f](https://doi.org/10.3847/1538-3881/aabc4f)
- Astropy Collaboration, Price-Whelan, A. M., Lim, P. L., et al. 2022, *ApJ*, 935, 167, doi: [10.3847/1538-4357/ac7c74](https://doi.org/10.3847/1538-4357/ac7c74)
- Barber, R. J., Tennyson, J., Harris, G. J., & Tolchenov, R. N. 2006, *MNRAS*, 368, 1087, doi: [10.1111/j.1365-2966.2006.10184.x](https://doi.org/10.1111/j.1365-2966.2006.10184.x)
- Barman, T. S., Hauschildt, P. H., & Allard, F. 2001, *ApJ*, 556, 885, doi: [10.1086/321610](https://doi.org/10.1086/321610)
- Barton, E. J., Yurchenko, S. N., & Tennyson, J. 2013, *MNRAS*, 434, 1469, doi: [10.1093/mnras/stt1105](https://doi.org/10.1093/mnras/stt1105)
- Bell, T. J., & Cowan, N. B. 2018, *ApJL*, 857, L20, doi: [10.3847/2041-8213/aabccc8](https://doi.org/10.3847/2041-8213/aabccc8)
- Beltz, H., Rauscher, E., Roman, M. T., & Guiliat, A. 2021, *AJ*, 163, 35
- Borysow, A. 1998, *Collision-induced Absorption in the Infrared: A Data Base for Modelling Planetary and Stellar Atmospheres*, Technical Report, Copenhagen Univ. Denmark Physics and Astrophysics
- Borysow, A. 2002, *A&A*, 390, 779, doi: [10.1051/0004-6361:20020555](https://doi.org/10.1051/0004-6361:20020555)
- Borysow, A., & Frommhold, L. 1989, *ApJ*, 341, 549, doi: [10.1086/167515](https://doi.org/10.1086/167515)
- Borysow, A., & Frommhold, L. 1990, *ApJL*, 348, L41, doi: [10.1086/185626](https://doi.org/10.1086/185626)
- Borysow, A., Frommhold, L., & Moraldi, M. 1989, *ApJ*, 336, 495, doi: [10.1086/167027](https://doi.org/10.1086/167027)
- Borysow, A., Jorgensen, U. G., & Fu, Y. 2001, *JQSRT*, 68, 235, doi: [10.1016/S0022-4073\(00\)00023-6](https://doi.org/10.1016/S0022-4073(00)00023-6)
- Borysow, A., Jorgensen, U. G., & Zheng, C. 1997, *A&A*, 324, 185
- Bourrier, V., Ehrenreich, D., Lendl, M., et al. 2020, *A&A*, 635, A205, doi: [10.1051/0004-6361/201936640](https://doi.org/10.1051/0004-6361/201936640)
- Buchner, J., Georgakakis, A., Nandra, K., et al. 2014, *A&A*, 564, A125, doi: [10.1051/0004-6361/201322971](https://doi.org/10.1051/0004-6361/201322971)
- Burrows, A., Budaj, J., & Hubeny, I. 2008, *ApJ*, 678, 1436, doi: [10.1086/533518](https://doi.org/10.1086/533518)
- Caffau, E., Ludwig, H. G., Steffen, M., Freytag, B., & Bonifacio, P. 2011, *SoPh*, 268, 255, doi: [10.1007/s11207-010-9541-4](https://doi.org/10.1007/s11207-010-9541-4)
- Caldas, A., Leconte, J., Selsis, F., et al. 2019, *A&A*, 623, A161, doi: [10.1051/0004-6361/201834384](https://doi.org/10.1051/0004-6361/201834384)
- Chubb, K. L., Rocchetto, M., Yurchenko, S. N., et al. 2021, *A&A*, 646, A21, doi: [10.1051/0004-6361/202038350](https://doi.org/10.1051/0004-6361/202038350)
- Delrez, L., Santerne, A., Almenara, J. M., et al. 2016, *MNRAS*, 458, 4025, doi: [10.1093/mnras/stw522](https://doi.org/10.1093/mnras/stw522)
- Drummond, B., Tremblin, P., Baraffe, I., et al. 2016, *A&A*, 594, A69, doi: [10.1051/0004-6361/201628799](https://doi.org/10.1051/0004-6361/201628799)
- Espinoza, N., & Jones, K. 2021, *AJ*, 162, 165, doi: [10.3847/1538-3881/ac134d](https://doi.org/10.3847/1538-3881/ac134d)
- Espinoza, N., Steinrueck, M. E., Kirk, J., et al. 2024, *Nature*, 632, 1017, doi: [10.1038/s41586-024-07768-4](https://doi.org/10.1038/s41586-024-07768-4)
- Evans, T. M., Sing, D. K., Kataria, T., et al. 2017, *Nature*, 548, 58, doi: [10.1038/nature23266](https://doi.org/10.1038/nature23266)
- Evans, T. M., Sing, D. K., Goyal, J. M., et al. 2018, *AJ*, 156, 283, doi: [10.3847/1538-3881/aaebff](https://doi.org/10.3847/1538-3881/aaebff)
- Evans-Soma, T. M., Sing, D. K., Barstow, J. K., et al. 2025, *NatAs*, submitted
- Falco, A., Leconte, J., Mechineau, A., & Pluriel, W. 2024, *A&A*, 685, A125, doi: [10.1051/0004-6361/202348880](https://doi.org/10.1051/0004-6361/202348880)
- Feroz, F., & Hobson, M. P. 2008, *MNRAS*, 384, 449, doi: [10.1111/j.1365-2966.2007.12353.x](https://doi.org/10.1111/j.1365-2966.2007.12353.x)
- Feroz, F., Hobson, M. P., & Bridges, M. 2009, *MNRAS*, 398, 1601, doi: [10.1111/j.1365-2966.2009.14548.x](https://doi.org/10.1111/j.1365-2966.2009.14548.x)
- Feroz, F., Hobson, M. P., Cameron, E., & Pettitt, A. N. 2019, *OJAp*, 2, 10, doi: [10.21105/astro.1306.2144](https://doi.org/10.21105/astro.1306.2144)
- Foreman-Mackey, D. 2016, *JOSS*, 1, 24, doi: [10.21105/joss.00024](https://doi.org/10.21105/joss.00024)
- Foreman-Mackey, D., Hogg, D. W., Lang, D., & Goodman, J. 2013, *PASP*, 125, 306, doi: [10.1086/670067](https://doi.org/10.1086/670067)
- Fortney, J. J., Lodders, K., Marley, M. S., & Freedman, R. S. 2008, *ApJ*, 678, 1419, doi: [10.1086/528370](https://doi.org/10.1086/528370)
- Goorvitch, D. 1994, *ApJS*, 95, 535, doi: [10.1086/192110](https://doi.org/10.1086/192110)
- Gordon, S., & McBride, B. J. 1994, *NASA Reference Publication*, 1311
- Goyal, J. M., Mayne, N., Sing, D. K., et al. 2018, *MNRAS*, 474, 5158, doi: [10.1093/mnras/stx3015](https://doi.org/10.1093/mnras/stx3015)
- Grant, D., & Wakeford, H. R. 2022, *Exo-TiC/ExoTiC-LD: ExoTiC-LD v3.0.0, v3.0.0*, Zenodo, Zenodo, doi: [10.5281/zenodo.7437681](https://doi.org/10.5281/zenodo.7437681)
- Grant, D., & Wakeford, H. R. 2023, *MNRAS*, 519, 5114, doi: [10.1093/mnras/stac3632](https://doi.org/10.1093/mnras/stac3632)
- Guillot, T. 2010, *A&A*, 520, A27, doi: [10.1051/0004-6361/200913396](https://doi.org/10.1051/0004-6361/200913396)
- Harris, C. R., Millman, K. J., van der Walt, S. J., et al. 2020, *Nature*, 585, 357, doi: [10.1038/s41586-020-2649-2](https://doi.org/10.1038/s41586-020-2649-2)
- Hauschildt, P. H., Allard, F., & Baron, E. 1999, *ApJ*, 512, 377, doi: [10.1086/306745](https://doi.org/10.1086/306745)
- Hoeijmakers, H. J., Seidel, J. V., Pino, L., et al. 2020, *A&A*, 641, A123, doi: [10.1051/0004-6361/202038365](https://doi.org/10.1051/0004-6361/202038365)
- Hoeijmakers, H. J., Kitzmann, D., Morris, B. M., et al. 2024, *A&A*, 685, A139, doi: [10.1051/0004-6361/202244968](https://doi.org/10.1051/0004-6361/202244968)
- Hunter, J. D. 2007, *CSE*, 9, 90, doi: [10.1109/MCSE.2007.55](https://doi.org/10.1109/MCSE.2007.55)
- Irwin, P. G. J., Teanby, N. A., de Kok, R., et al. 2008, *JQSRT*, 109, 1136, doi: [10.1016/j.jqsrt.2007.11.006](https://doi.org/10.1016/j.jqsrt.2007.11.006)

- Jaziri, A. Y., Pluriel, W., Bocchieri, A., et al. 2024, *A&A*, 684, A25, doi: [10.1051/0004-6361/202347379](https://doi.org/10.1051/0004-6361/202347379)
- John, T. L. 1988, *A&A*, 193, 189
- Jones, K., & Espinoza, N. 2022, *JOSS*, 7, 2382, doi: [10.21105/joss.02382](https://doi.org/10.21105/joss.02382)
- Kipping, D. M., & Tinetti, G. 2010, *MNRAS*, 407, 2589, doi: [10.1111/j.1365-2966.2010.17094.x](https://doi.org/10.1111/j.1365-2966.2010.17094.x)
- Kitzmann, D., Heng, K., Rimmer, P. B., et al. 2018, *ApJ*, 863, 183
- Kreidberg, L. 2015, *PASP*, 127, 1161, doi: [10.1086/683602](https://doi.org/10.1086/683602)
- Kurucz, R. L. 1994, in *IAU Colloq. 146: Molecules in the Stellar Environment*, ed. U. G. Jorgensen, Vol. 428, 282, doi: [10.1007/3-540-57747-5_51](https://doi.org/10.1007/3-540-57747-5_51)
- Lacis, A. A., & Oinas, V. 1991, *J. Geophys. Res.*, 96, 9027, doi: [10.1029/90JD01945](https://doi.org/10.1029/90JD01945)
- Lee, J. M., Fletcher, L. N., & Irwin, P. G. J. 2012, *MNRAS*, 420, 170, doi: [10.1111/j.1365-2966.2011.20013.x](https://doi.org/10.1111/j.1365-2966.2011.20013.x)
- Lewis, N. K., Wakeford, H. R., MacDonald, R. J., et al. 2020, *ApJL*, 902, L19, doi: [10.3847/2041-8213/abb77f](https://doi.org/10.3847/2041-8213/abb77f)
- Li, G., Gordon, I. E., Rothman, L. S., et al. 2015, *ApJS*, 216, 15, doi: [10.1088/0067-0049/216/1/15](https://doi.org/10.1088/0067-0049/216/1/15)
- Line, M. R., Zhang, X., Vasisht, G., et al. 2012, *ApJ*, 749, 93, doi: [10.1088/0004-637X/749/1/93](https://doi.org/10.1088/0004-637X/749/1/93)
- Line, M. R., Wolf, A. S., Zhang, X., et al. 2013, *ApJ*, 775, 137, doi: [10.1088/0004-637X/775/2/137](https://doi.org/10.1088/0004-637X/775/2/137)
- Lothringer, J. D., Barman, T., & Koskinen, T. 2018, *ApJ*, 866, 27, doi: [10.3847/1538-4357/aadd9e](https://doi.org/10.3847/1538-4357/aadd9e)
- Lothringer, J. D., & Barman, T. S. 2020, *AJ*, 159, 289, doi: [10.3847/1538-3881/ab8d33](https://doi.org/10.3847/1538-3881/ab8d33)
- Lothringer, J. D., Fu, G., Sing, D. K., & Barman, T. S. 2020, *ApJL*, 898, L14, doi: [10.3847/2041-8213/aba265](https://doi.org/10.3847/2041-8213/aba265)
- Lothringer, J. D., Rustamkulov, Z., Sing, D. K., et al. 2021, *ApJ*, 914, 12, doi: [10.3847/1538-4357/abf8a9](https://doi.org/10.3847/1538-4357/abf8a9)
- Lothringer, J. D., Sing, D. K., Rustamkulov, Z., et al. 2022, *Nature*, 604, 49, doi: [10.1038/s41586-022-04453-2](https://doi.org/10.1038/s41586-022-04453-2)
- Magic, Z., Chiavassa, A., Collet, R., & Asplund, M. 2015, *A&A*, 573, A90, doi: [10.1051/0004-6361/201423804](https://doi.org/10.1051/0004-6361/201423804)
- McBride, B. J. 1993, *National Aeronautics and Space Administration, Office of Management, Scientific and Technical Information Program*, 4513
- McKinney, W. 2010, *Data Structures for Statistical Computing in Python*, doi: [10.25080/Majora-92bf1922-00a](https://doi.org/10.25080/Majora-92bf1922-00a)
- Mikal-Evans, T., Sing, D. K., Kataria, T., et al. 2020, *MNRAS*, 496, 1638, doi: [10.1093/mnras/staa1628](https://doi.org/10.1093/mnras/staa1628)
- Mikal-Evans, T., Sing, D. K., Goyal, J. M., et al. 2019, *MNRAS*, 488, 2222
- Mikal-Evans, T., Sing, D. K., Barstow, J. K., et al. 2022, *NatAs*, 6, 471, doi: [10.1038/s41550-021-01592-w](https://doi.org/10.1038/s41550-021-01592-w)
- Mikal-Evans, T., Sing, D. K., Dong, J., et al. 2023, *ApJL*, 943, L17, doi: [10.3847/2041-8213/acb049](https://doi.org/10.3847/2041-8213/acb049)
- Morello, G., Zingales, T., Martin-Lagarde, M., Gastaud, R., & Lagage, P.-O. 2021, *AJ*, 161, 174, doi: [10.3847/1538-3881/abe048](https://doi.org/10.3847/1538-3881/abe048)
- Murphy, M. M., Beatty, T. G., Schlawin, E., et al. 2024, *NatAs*, 8, 1562, doi: [10.1038/s41550-024-02367-9](https://doi.org/10.1038/s41550-024-02367-9)
- Newville, M., Stensitzki, T., Allen, D. B., & Ingargiola, A. 2015, *LMFIT: Non-Linear Least-Square Minimization and Curve-Fitting for Python, 0.8.0*, Zenodo, doi: [10.5281/zenodo.11813](https://doi.org/10.5281/zenodo.11813)
- Parmentier, V., Line, M. R., Bean, J. L., et al. 2018, *A&A*, 617, A110, doi: [10.1051/0004-6361/201833059](https://doi.org/10.1051/0004-6361/201833059)
- Pluriel, W., Zingales, T., Leconte, J., & Parmentier, V. 2020, *A&A*, 636, A66, doi: [10.1051/0004-6361/202037678](https://doi.org/10.1051/0004-6361/202037678)
- Polyansky, O. L., Kyuberis, A. A., Zobov, N. F., et al. 2018, *MNRAS*, 480, 2597, doi: [10.1093/mnras/sty1877](https://doi.org/10.1093/mnras/sty1877)
- Richard, C., Gordon, I. E., Rothman, L. S., et al. 2012, *JQSRT*, 113, 1276, doi: [10.1016/j.jqsrt.2011.11.004](https://doi.org/10.1016/j.jqsrt.2011.11.004)
- Rothman, L., Gordon, I., Barber, R., et al. 2010, *JQSRT*, 111, 2139, doi: [https://doi.org/10.1016/j.jqsrt.2010.05.001](https://doi.org/https://doi.org/10.1016/j.jqsrt.2010.05.001)
- Rustamkulov, Z., Sing, D. K., Liu, R., & Wang, A. 2022, *ApJL*, 928, L7, doi: [10.3847/2041-8213/ac5b6f](https://doi.org/10.3847/2041-8213/ac5b6f)
- Rustamkulov, Z., Sing, D. K., Mukherjee, S., et al. 2023, *Nature*, 614, 659, doi: [10.1038/s41586-022-05677-y](https://doi.org/10.1038/s41586-022-05677-y)
- Sing, D. K., Rustamkulov, Z., Thorngren, D. P., et al. 2024, *Nature*, 630, 831, doi: [10.1038/s41586-024-07395-z](https://doi.org/10.1038/s41586-024-07395-z)
- Skilling, J. 2004, in *American Institute of Physics Conference Series*, Vol. 735, *Bayesian Inference and Maximum Entropy Methods in Science and Engineering: 24th International Workshop on Bayesian Inference and Maximum Entropy Methods in Science and Engineering*, ed. R. Fischer, R. Preuss, & U. V. Toussaint, 395–405, doi: [10.1063/1.1835238](https://doi.org/10.1063/1.1835238)
- Speagle, J. S. 2020, *MNRAS*, 493, 3132, doi: [10.1093/mnras/staa278](https://doi.org/10.1093/mnras/staa278)
- Ter Braak, C. J. F. 2006, *Statistics and Computing*, 16, 239, doi: [10.1007/s11222-006-8769-1](https://doi.org/10.1007/s11222-006-8769-1)
- ter Braak, C. J. F., & Vrugt, J. A. 2008, *Statistics and Computing*, 18, 435, doi: [10.1007/s11222-008-9104-9](https://doi.org/10.1007/s11222-008-9104-9)
- Tremblin, P., Amundsen, D. S., Chabrier, G., et al. 2016, *ApJL*, 817, L19, doi: [10.3847/2041-8205/817/2/L19](https://doi.org/10.3847/2041-8205/817/2/L19)
- Tremblin, P., Amundsen, D. S., Mourier, P., et al. 2015, *ApJL*, 804, L17, doi: [10.1088/2041-8205/804/1/L17](https://doi.org/10.1088/2041-8205/804/1/L17)
- Tremblin, P., Chabrier, G., Mayne, N. J., et al. 2017, *ApJ*, 841, 30, doi: [10.3847/1538-4357/aa6e57](https://doi.org/10.3847/1538-4357/aa6e57)
- Virtanen, P., Gommers, R., Oliphant, T. E., et al. 2020, *NatMe*, 17, 261, doi: [10.1038/s41592-019-0686-2](https://doi.org/10.1038/s41592-019-0686-2)

Wardenier, J. P., Parmentier, V., Line, M. R., & Lee, E. K. H. 2023, MNRAS, 525, 4942, doi: [10.1093/mnras/stad2586](https://doi.org/10.1093/mnras/stad2586)

Wardenier, J. P., Parmentier, V., Line, M. R., et al. 2024, PASP, 136, 084403, doi: [10.1088/1538-3873/ad5c9f](https://doi.org/10.1088/1538-3873/ad5c9f)

Winn, J. N. 2010, in Exoplanets, ed. S. Seager (University of Arizona Press, Tucson, AZ, USA), 55–77, doi: [10.48550/arXiv.1001.2010](https://doi.org/10.48550/arXiv.1001.2010)

Yurchenko, S. N., Mellor, T. M., Freedman, R. S., & Tennyson, J. 2020, MNRAS, 496, 5282, doi: [10.1093/mnras/staa1874](https://doi.org/10.1093/mnras/staa1874)

Yurchenko, S. N., Sinden, F., Lodi, L., et al. 2018, MNRAS, 473, 5324, doi: [10.1093/mnras/stx2738](https://doi.org/10.1093/mnras/stx2738)

APPENDIX

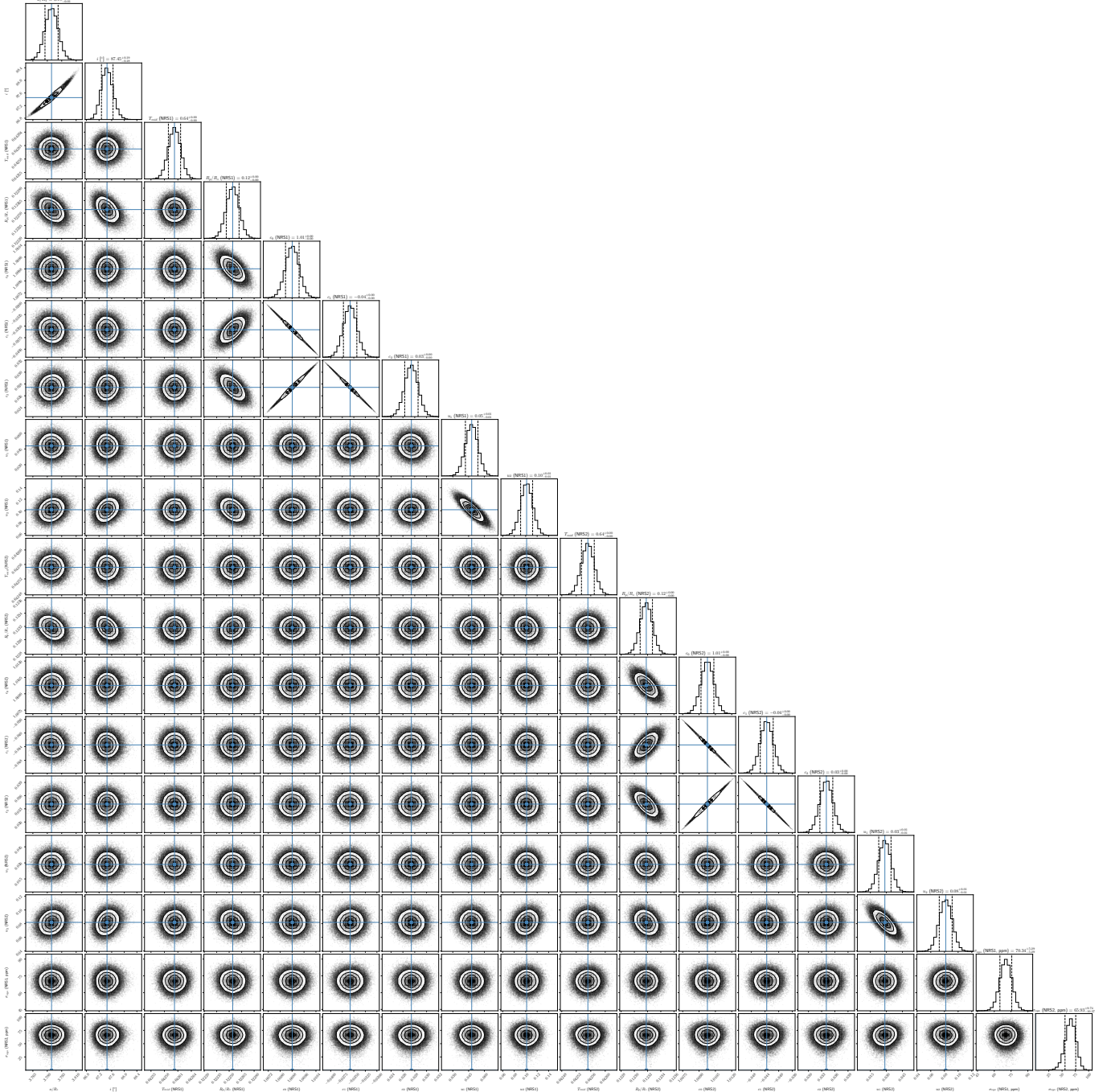


Figure 12. Posterior probabilities for the fit parameters of the simultaneous fit to both detectors' white light curves. For a description of each parameter, see Table 1.

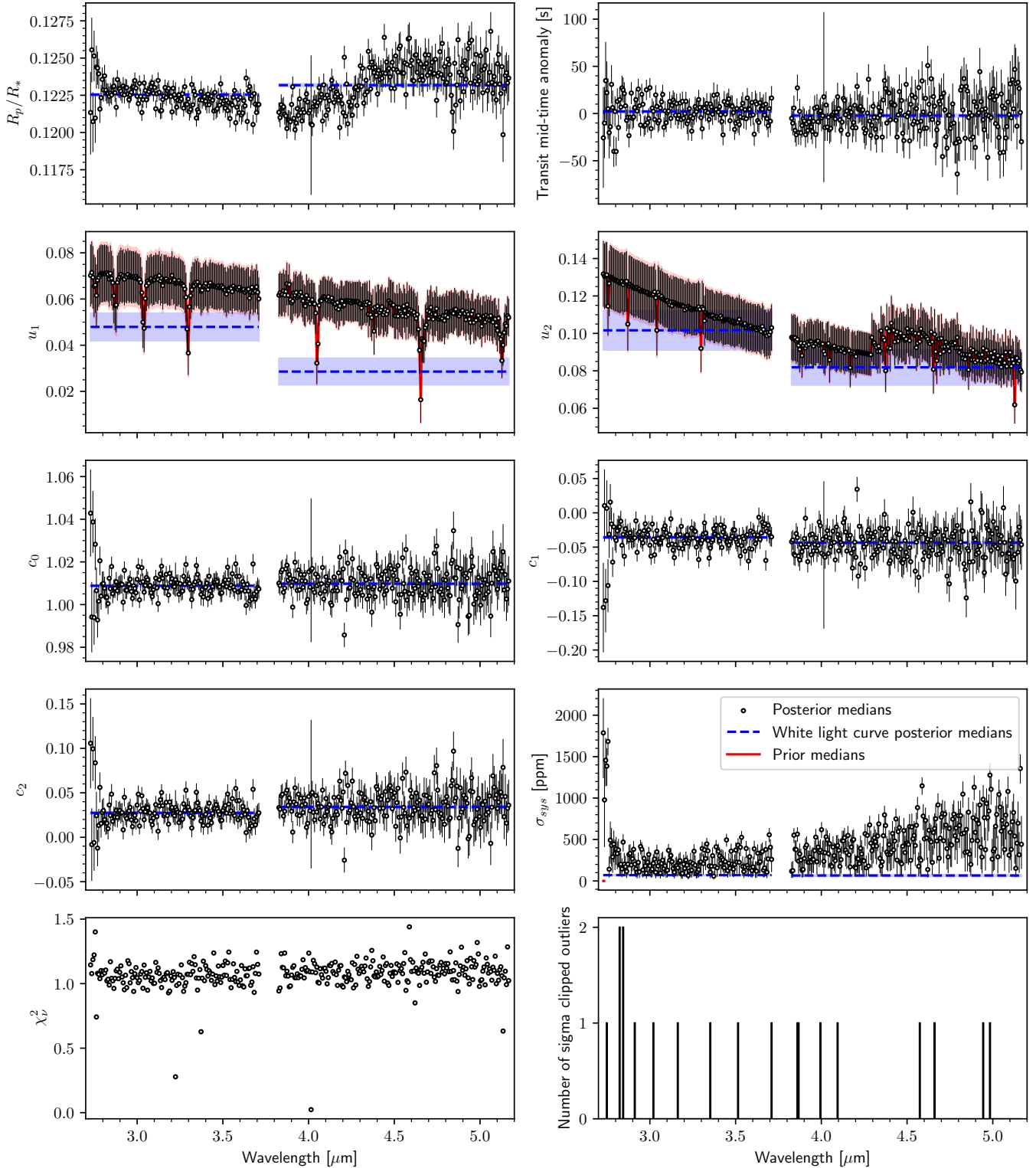


Figure 13. MCMC results for the fits to the spectrophotometric transit-only light curves at $R \sim 600$. For the fit parameters, we indicate the medians and 1σ intervals of the white light curve fit’s posteriors (see Table 1) for both the NRS1 and NRS2 detectors using dashed blue lines and shaded blue regions. For the limb darkening parameters (u_1 and u_2), we adopted Gaussian priors, whose μ and σ are shown using solid red lines and red shadings, respectively. The transit midtimes were subtracted by their median.

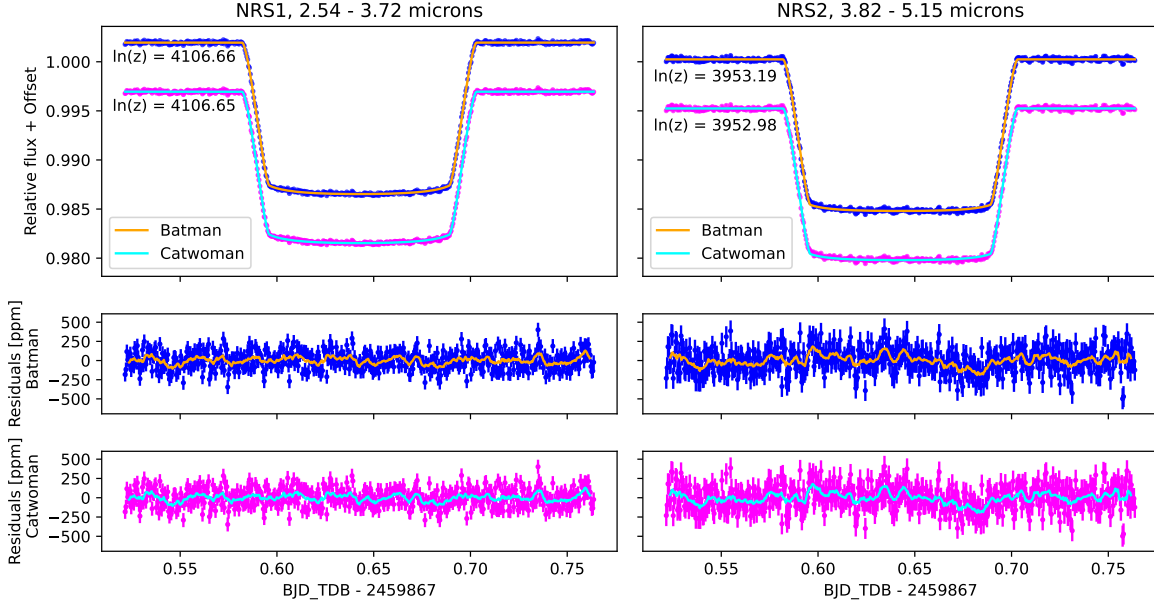


Figure 14. Fits to the white light curves using *batman* and *catwoman* models.

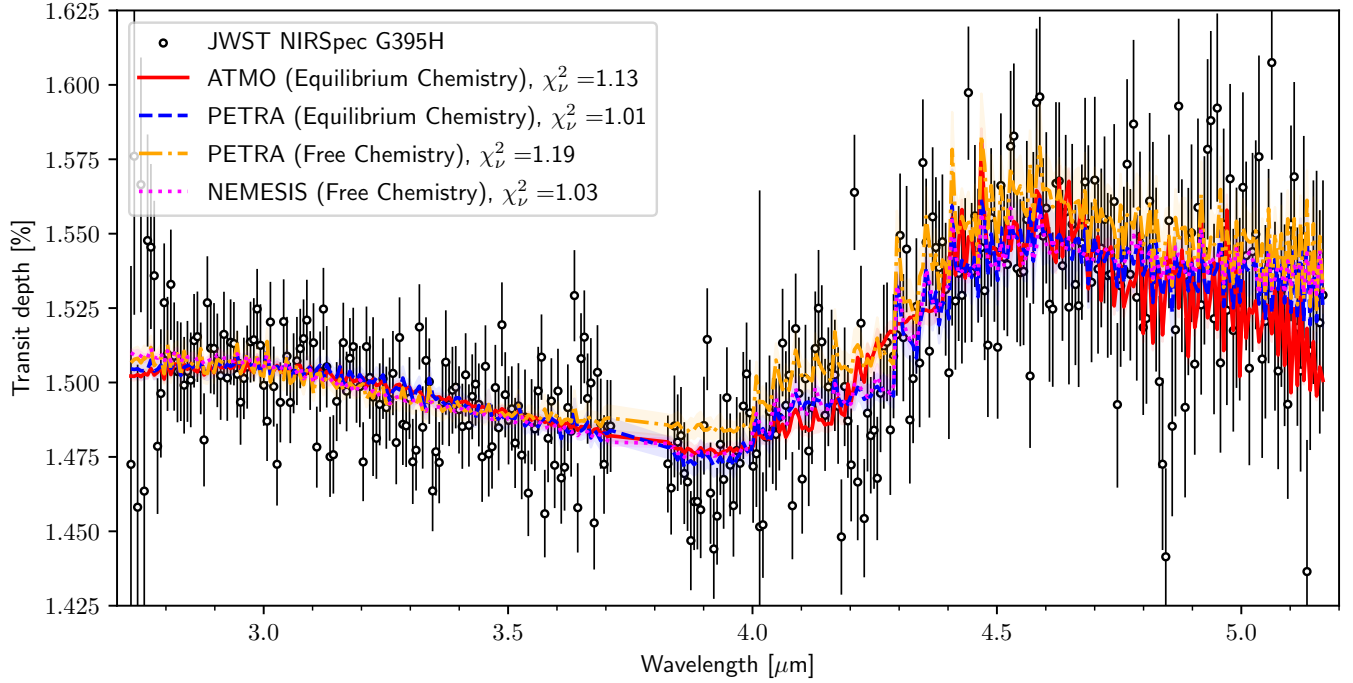


Figure 15. Transmission spectrum at $R \sim 600$ obtained from the transit-only analysis along with the median model spectra of the applied retrievals. The 1σ intervals of the model spectra are illustrated using shaded regions.

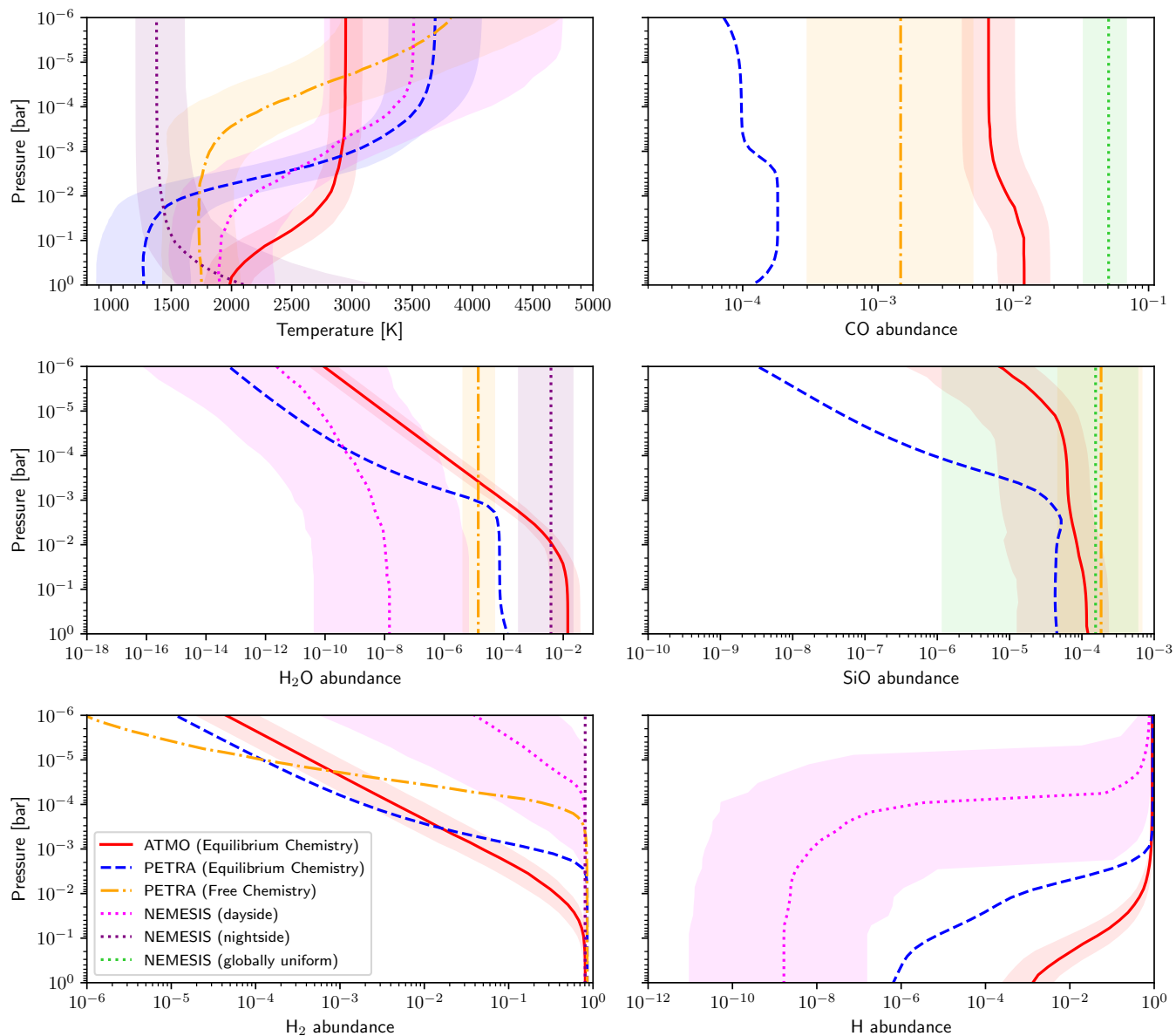


Figure 16. Results from the retrievals applied to WASP-121 b’s transmission spectrum obtained from the transit-only analysis. The temperature and abundance profiles inferred from the different retrievals are depicted using lines with shaded regions indicating the extent of the corresponding 1σ regions. All NEMESIS results shown here were inferred from a simultaneous retrieval of both hemispheres. Any atmospheric variable varied between the hemispheres in that framework is presented using dotted magenta and purple lines, while the molecular abundances that are held identical in both hemispheres are shown using dotted green lines.